First Measurement of the Transverse-Target Single-Spin Asymmetry in Exclusive Muon-Production of ρ^0 Mesons at COMPASS

Jasmin Kiefer

PHYSIKALISCHES INSTITUT
ALBERT-LUDWIGS-UNIVERSITÄT FREIBURG

First Measurement of the Transverse-Target Single-Spin Asymmetry in Exclusive Muon-Production of ρ^0 Mesons at COMPASS

Diplomarbeit

vorgelegt von

Jasmin Kiefer

aus Schönau im Schwarzwald

Fakultät für Mathematik und Physik

Albert-Ludwigs-Universität

Freiburg im Breisgau

August 2007

Contents

1 Introduction

For almost a century, protons and neutrons have been known as particles carrying half-integer spin. Their non-pointlike nature was revealed by measurements of their anomalous magnetic moments and deep inelastic scattering experiments lead to the discovery of partons. The charged constituents of the nucleon were identified with the theoretically predicted quarks [1, 2], which carry half-integer spin themselves. Consequently, the question about their helicity contributions to the nucleon spin arose. First experimental investigations by the European Muon Collaboration (EMC), however, determined the quark helicity contribution to be compatible with zero [3] and therewith far below the anticipated value. This *Spin-Crisis* triggered further experimental investigations, leading to a measured quark helicity contribution of about 30%. Thus, the fundamental question of contributions to the nucleon spin remained unsolved.

In 1992, with the advanced methods of the field theory of strong interaction Quantum Chromodynamics (QCD), Jaffe and Manohar introduced a sum rule [4]. Therein, the spin of the nucleon can be decomposed as

$$\frac{1}{2}\hbar = \frac{1}{2}\Delta\Sigma + \Delta G + L_q + L_g \quad , \tag{1.1}$$

where $\Delta\Sigma$ and L_q denote the helicity and orbital angular momentum contributions of quarks and anti-quarks and ΔG and L_g the corresponding contributions of gluons.

The helicity contribution $\Delta\Sigma$ has already been determined with high accuracy [5] and the helicity contribution of gluons ΔG is presently under experimental investigation [6]. Still remaining is the question of how the orbital angular momenta of quarks and gluons contribute to the spin of the nucleon. In 1996, Generalized Parton Distributions (GPDs) [7, 8], appearing in exclusive scattering processes, raised the interest of a wide community. The huge potential of studying these generalized parton distributions to reveal the spin structure of the nucleon was pointed out in a work by Ji [9]. Therein, GPDs fulfill a sum rule which may provide access to the contributions of total angular momenta J^q carried by quarks. Thus, with additional knowledge of the helicity contributions, the missing piece of information on the orbital angular momentum contribution L_q to the nucleon spin might become accessible.

The experimental access to Generalized Parton Distributions is a rather advanced task and started only recently. Hard exclusive processes are a promising tool to study these so far unknown functions. One special channel in this wide range of scattering processes is the hard exclusive production of ρ^0 vector mesons on a transversely polarized target. Of high interest in this context is the transverse-target single-spin asymmetry $A_{\mathrm{UT}}(\phi_h - \phi_S)$, depending on the azimuthal angle ϕ_h of the meson production plane and ϕ_S of the target spin vector with respect to the lepton scattering plane. This azimuthal asymmetry provides access to the generalized parton distribution E, appearing in Ji's sum rule, which is otherwise hardly determinable.

This thesis is dedicated to the extraction of the amplitude $A_{\mathrm{UT}}^{\sin(\phi_h-\phi_S)}$ of the transverse-target single-spin asymmetry $A_{\mathrm{UT}}(\phi_h - \phi_S)$ in hard exclusive ρ^0 meson production on a transversely polarized deuteron target. For understanding the meaning of this quantity, the formalism and properties of generalized parton distributions are presented in Chapter 2. Beside the description of the transverse-target single-spin asymmetry, further experimental observables for accessing generalized parton distributions are discussed. Presently, the COMPASS (**CO**mmon **M**uon and **P**roton **A**pparatus for **S**tructure and **S**pectroscopy) experiment is the only experimental facility to study the amplitude $A_{\mathrm{UT}}^{\sin(\phi_h-\phi_S)}$ in hard exclusive meson production on a transversely polarized deuteron target. Hence, a brief description of the experimental setup is presented in Chapter 3. In addition to exclusive production of ρ^0 mesons, the data recorded within the COMPASS experiment contain events for the analyses of other experimental observables. Consequently, a particular data sample, consisting of hard exclusively produced ρ^0 mesons, needs to be selected. The detailed description of this procedure is given in Chapter 4, accompanied by a presentation of the properties of the finally selected data sample. For the extraction of the amplitude $A_{\mathrm{UT}}^{\sin(\phi_h-\phi_S)}$ from this final data sample, a dedicated algorithm is needed, which is presented in Chapter 5. Finally, the very first results obtained for the amplitude of the transverse-target single-spin asymmetry are presented and discussed in Chapter 6.

2 Theoretical Motivation

Deep inelastic scattering (DIS) of leptons on nuclei is the archetype of all hard reactions involving the concept of parton distribution functions (PDFs). The description of such processes is therefore a convenient starting point (cf. Section 2.1) for the introduction of Generalized Parton Distributions (GPDs) in Section 2.2. Two experimental possibilities to access these so far unexplored quantities are presented, Deeply Virtual Compton Scattering (DVCS) in Section 2.3 and Hard Exclusive Meson Production (HEMP) in Section 2.4. Special attention is paid to the transverse-target single-spin asymmetry $A_{\mathrm{UT}}(\phi_h - \phi_S)$, described in Section 2.4.1. One process, in which this observable appears is the exclusive muon-production of longitudinally polarized ρ^0 mesons. Using this process, the amplitude $A_{\mathrm{UT}}^{\sin(\phi_h-\phi_S)}$ of the transverse-target single-spin asymmetry is extracted in this thesis.

2.1 Deep Inelastic Scattering

2.1.1 General Information

In the inclusive scattering process of a high-energetic lepton $l(k, s)$ on a nucleon target $N(P, S)$, characterized by their four-momenta (k and P) and spin vectors (s and S), the scattered lepton $l(k', s')$ is detected, while the nucleon fragments into an undetected final hadronic state X (cf. Figure 2.1)

$$l(k, s) + N(P, S) \rightarrow l(k', s') + X \quad . \tag{2.1}$$

The lepton-nucleon interaction in this process is mediated by the exchange of a highly virtual gauge boson: a photon, Z or W boson. Due to the specific energy range covered by the COMPASS experiment (cf. Section 4.6), this interaction can be solely described in terms of the electromagnetic force [10]. Therefore, the process (2.1) can also be described by:

$$\gamma^*(q, \sigma) + N(P, S) \rightarrow X \quad , \tag{2.2}$$

where q and σ denote the four-momentum and the spin vector of the virtual photon γ^*. Using the optical theorem, this photon-nucleon interaction can be related to the imaginary part of the forward Compton amplitude (cf. square of the handbag diagram depicted in Figure 2.2).

The inclusive scattering process (2.2) is governed by the kinematic variables

$$Q^2 = -q^\mu q_\mu = -(k - k')^2 \text{ and} \tag{2.3}$$
$$\nu = P^\mu q_\mu \ , \tag{2.4}$$

where a summation over equal indices is performed.

In the Bjorken limit, i.e. when the photon virtuality Q^2 and ν both become large ($Q^2, \nu \to \infty$) with the ratio $x_{Bj} = Q^2/2M\nu$ remaining fixed, where M denotes the mass of the target nucleon, the inclusive scattering process (2.2) can be divided into a hard leptonic and a soft hadronic sub-process (cf. Fig. 2.1). The proof of validity for this factorization was given in Ref. [11].

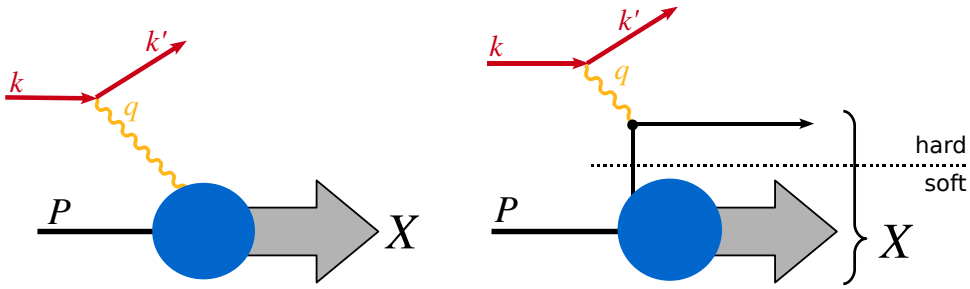

Figure 2.1: The diagram shows the lepton-nucleon scattering process, mediated by the exchange of a virtual photon, and the production of an undetected final state X. On the left hand side, a phenomenological picture of the DIS process is given, whereas the right figure shows the scattering process in the partonic picture. Therein, the photon scatters on one individual quark. This second approach is only valid in the Bjorken limit, where the concept of factorization can be applied.

The term factorization can be better understood by looking at the double-differential cross section of the inclusive lepton scattering process. In leading order of the electromagnetic fine-structure constant α_{em}, this double-differential cross section can be written as a product of the leptonic tensor $L_{\mu\nu}$ and the hadronic tensor $W_{\mu\nu}$ [12]

$$\frac{d^2\sigma}{d\Omega dE'} = \frac{\alpha_{\text{em}}}{Q^4}\frac{E'}{E} L_{\mu\nu} W^{\mu\nu} \ , \tag{2.5}$$

where E and E' denote the energies of the incident and scattered beam particles and Ω is the solid angle in which the scattered lepton is detected. While

the leptonic sub-process, represented by $L_{\mu\nu}$, can be calculated in perturbative Quantum Electro Dynamics (pQED) [13], the soft hadronic sub-process cannot be treated with perturbative methods. Instead, the hadronic tensor $W_{\mu\nu}$ can be parameterized in terms of *a priori* unknown functions, represented by the large blobs in Figure 2.1 and 2.2.

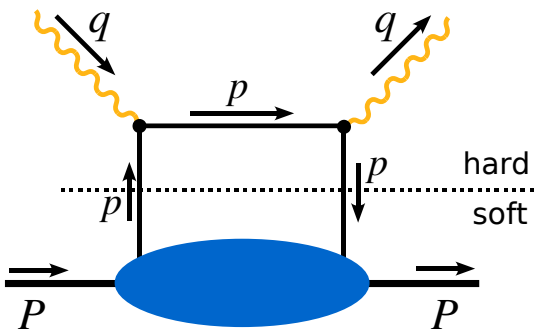

Figure 2.2: Handbag diagram [14], corresponding to the deep inelastic scattering processes $\gamma^* N \rightarrow X$ in leading order of the strong coupling constant $\alpha_s(Q^2)$. The factorization into a hard leptonic and soft hadronic sub-process, valid in the Bjorken limit, is indicated by the dotted line. The parton distribution functions, used for parameterization of the nucleon in the hadronic sub-process, are represented by the lower blob.

2.1.2 Parton Distribution Functions (PDFs)

Using the concept of factorization, the cross section (2.5) can be rewritten as a convolution of the scattering cross section on a point-like parton with a parton distribution function $f^{q/N}(x)$, defined for each quark flavor $q = u, \bar{u}, d, \bar{d}, s, \bar{s}, \ldots$ in a target nucleon N [12]

$$\frac{d^2\sigma^{lN\rightarrow l'X}}{dQ^2 dx_{Bj}} = \sum_q \int_x^1 d\xi \; f^{q/N}(\xi) \cdot \frac{d^2\sigma^{lq\rightarrow l'q'}}{dQ^2 d\xi} + \text{terms in higher order} \tag{2.6}$$

In unpolarized deep inelastic scattering, by using the optical theorem (cf. Section 2.1.1), the parton distributions $f^{q/N}(x)$ can be interpreted as a probability density for finding a parton of specific momentum fraction x in the target nucleon. In the Infinite-Momentum-Frame of the nucleon, x can be interpreted as the fraction of the nucleon momentum carried by one individual parton.

For experimental investigations, the deep inelastic scattering cross section (2.6) can be expressed in terms of observable structure functions, e.g. in the case of unpolarized lepton-nucleon scattering, the cross section can be written using the unpolarized structure functions $F_1(\nu, Q^2)$ and $F_2(\nu, Q^2)$

$$\frac{d^2\sigma}{d\Omega dE'} = \frac{4E'^2\alpha_{\mathrm{em}}}{Q^4}\left\{\frac{1}{M_N}\sin^2\left(\frac{\Theta}{2}\right)F_1(\nu,Q^2) + \frac{1}{\nu}\cos^2\left(\frac{\Theta}{2}\right)F_2(\nu,Q^2)\right\} \quad . \tag{2.7}$$

Just like the cross section itself, these two functions depend, in the Bjorken limit, only on the variable x_{Bj} and not on the two variables ν and Q^2 independently. By using the Callan-Gross relation [15], the observable structure functions and the theoretically constructed PDFs can be related in the context of the Quark Parton Model [16] via:

$$2F_1(x_{Bj}) = \frac{F_2(x_{Bj})}{x_{Bj}} = \sum_q e_q^2\, f_1^q(x_{Bj}) \quad , \tag{2.8}$$

where e_q denotes the charge of a parton of flavor q. A more convenient notation for the parton distribution function $f_1^q(x)$ (in unpolarized DIS) is $q(x)$, e.g. $u(x)$ for the u quark. As in equation (2.8), the parton *helicity* distribution functions $\Delta\, q(x)$ and the spin-dependent structure functions $g_1(x)$, both appearing in polarized deep inelastic scattering, can be related via:

$$g_1(x_{Bj}) = \frac{1}{2}\sum_a e_a^2\, \Delta\, q(x_{Bj}) \quad . \tag{2.9}$$

2.2 Generalized Parton Distributions (GPDs)

The concept of generalized parton distributions, and their huge potential for studying the nucleon structure to a hitherto impossible extent, was introduced in theoretical works by Müller *et al.* [7], Radyushkin [8] and Ji [9]. Detailed reviews on Generalized Parton Distributions can be found in Ref. [17, 18].

The factorization of dynamics into soft and hard sub-processes is not limited to deep inelastic scattering, but can also be applied to the more general case of finite momentum transfer to the target. The proof of validity for applying factorization in Deeply Virtual Compton Scattering (DVCS) (cf. left-hand side of Fig. 2.3) was given in Ref. [19, 20], while for hard exclusive meson production (HEMP) (cf. right-hand side of Fig. 2.3), the corresponding proof can be found in Ref. [21]. But before describing these processes in more detail in Section 2.3 and 2.4, the concept of parton distribution functions, as used for the description

of inclusive deep inelastic scattering processes, is generalized for exclusive processes. Therein once again *a priori* unknown functions, the *generalized* parton distributions (GPDs) appear.

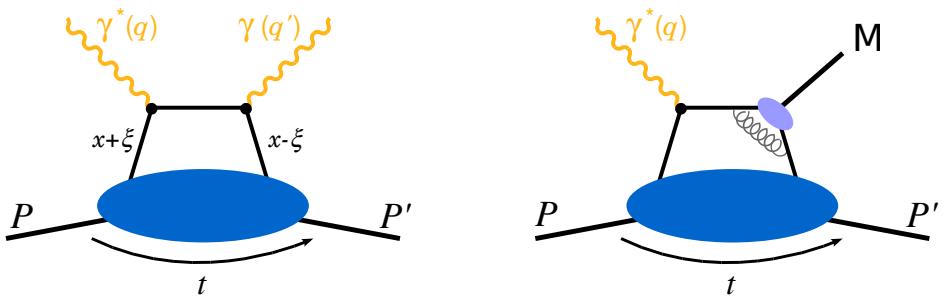

Figure 2.3: Illustrated are the handbag diagrams for deeply virtual Compton scattering (left) and hard exclusive meson production (right). Similar to the diagram for deep inelastic scattering, the large blobs represent parton distributions, but in this case *generalized* parton distributions. The finite momentum transfer to the target nucleon is indicated by the curved arrow, labeled with the four-momentum transfer t. The upper light blue blob represents a meson distribution amplitude.

2.2.1 Generalization Of Parton Distribution Functions

The factorization theorem asserts that the amplitude of exclusive[1] reactions can be written as a convolution of generalized parton distributions $\mathbf{f}_q$ with hard scattering coefficients C_q [2], where the latter can be computed as a power series [23, 24] in the strong coupling constant $\alpha_s(Q^2)$,

$$\sum_q \int_{-1}^{1} dx\, \mathbf{f}_q(x,\xi,t) \cdot C_q(x,\xi,Q^2,\ldots) \quad . \tag{2.10}$$

The hard scattering coefficients and the distribution functions are defined for each quark flavor q and for gluons. The generalized parton distributions $\mathbf{f}_q(x,\xi,t)$ depend on three kinematic variables, the fractions x and ξ of longitudinal momentum of the nucleon carried by a parton and the squared four-momentum transfer t between the initial and final nucleon states. The so-called skewedness variable

[1] The term *exclusive* is used for scattering processes where every final state particle is detected.

[2] For a full definition of the amplitude in hard exclusive meson production, additional terms are needed. These are the so-called meson distribution amplitudes, represented by the light blue blob in the upper right part of Figure 2.3. Further information about distribution amplitudes can be found in Ref. [17, 22].

ξ and the Mandelstam variable t are defined by:

$$\xi = \frac{x_{Bj}}{(1 - x_{Bj}/2)} \tag{2.11}$$

$$t \overset{def}{=} (P - P')^2 = \Delta^2 \ . \tag{2.12}$$

The definition of ξ in this form is however only valid in the Bjorken limit. For complete definitions of ξ and x light-cone coordinates are needed. A detailed review about light-cone variables can be found in Ref. [25] and in Chapter 2 of Ref. [18].

2.2.2 Forward Limit

Comparing equation (2.10) with equation (2.6), the connection between usual parton distributions and their generalized counterparts is directly evident. However, an important difference between GPDs and usual PDFs is, that the initial and final nucleon states in exclusive scattering processes are not necessarily equal, but can differ in their momenta and helicities. Additionally, it should be emphasized, that the factorization in exclusive reactions takes place at the amplitude level of the process, while in DIS the cross section itself factorizes, which leads to probabilistic interpretations. Nevertheless, the term *generalization* indicates that there is a specific limit in which the generalized parton distributions reduce to the usual parton distribution functions. This specific limit is called the forward limit, characterized by:

$$t = 0 \qquad \text{and} \qquad \xi = 0 \ , \tag{2.13}$$

where the four-momenta of the initial and final nucleon states and their helicities are equal. The generalized parton distributions $\mathbf{f}_q(x, \xi, t) \overset{2.13}{=} \mathbf{f}_q(x, 0, 0)$, can then be related to the spin-independent or spin-dependent quark densities $q(x)$ and $\Delta q(x)$, obtained from DIS processes, via:

$$\begin{aligned}
\text{for } x > 0\text{:} \quad H^q(x,0,0) &= q(x), & \tilde{H}^q(x,0,0) &= \Delta\, q(x) \\
\text{for } x < 0\text{:} \quad H^q(x,0,0) &= -\bar{q}(-x), & \tilde{H}^q(x,0,0) &= \Delta\, \bar{q}(-x)
\end{aligned}$$

where H^q and $\tilde{H}^q$ are written in the most convenient notations for two out of four (quark chirality conserving) generalized distribution functions: E^q, H^q, $\tilde{E}^q$ and $\tilde{H}^q$. In the region $x > 0$, the GPDs H and $\tilde{H}$ are reduced to quark distribution functions, while the relations for $x < 0$ hold for anti-quark distributions. In contrast to H and $\tilde{H}$, the generalized parton distributions E and $\tilde{E}$ are not measurable in DIS. Consequently, there is no corresponding relation between these

functions and usual parton distribution functions. The reason for this lack of relation can be understood in two ways:

- Using the additional information, that both functions are multiplied by a kinematic factor proportional to $\Delta = \sqrt{t}$, in their defining equation. Therefore (at $t = 0$), these GPDs decouple in the forward limit. Consequently, information about these two generalized parton distribution functions at $\xi = t = 0$ can not be accessed in processes, where parton distributions appear in the cross section via the optical theorem.

- While H^q and $\tilde{H}^q$ conserve the helicity of the nucleon in exclusive reactions, E^q and $\tilde{E}^q$ permit the possibility that the nucleon helicity is flipped. In this case, the overall helicity is not conserved, because the helicity of the (massless) quark cannot be flipped. Thus, angular momentum conservation has to be ensured by a transfer of *orbital* angular momentum, which is of course only possible for a finite transfer of transverse momentum. Consequently, this process cannot be observed within ordinary parton distributions, where the momenta of the initial and final nucleon states are equal.

Beside the reduction of GPDs to usual PDFs in the forward limit, the first moments of generalized parton distributions are connected to elastic form factors of the nucleon [26]. For a particular quark of flavor q and an arbitrary value of the skewedness ξ, this relation is given by [27]:

$$\int_{-1}^{1} dx\ H^q(x,\xi,t) = F_1^q(t) \tag{2.14}$$

$$\int_{-1}^{1} dx\ E^q(x,\xi,t) = F_2^q(t) \tag{2.15}$$

$$\int_{-1}^{1} dx\ \tilde{H}^q(x,\xi,t) = g_{\mathrm{A}}^q(t) \tag{2.16}$$

$$\int_{-1}^{1} dx\ \tilde{E}^q(x,\xi,t) = h_{\mathrm{A}}^q(t) \tag{2.17}$$

where $F_{1,2}^q$, g_{A}^q and h_{A}^q represent the Dirac, Pauli, axial and pseudo-scalar elastic form factors, respectively.

2.2.3 Sum Rule

One fundamental question about the nucleon structure, which is not accessible in deep inelastic scattering, is how the total spin of the nucleon is made up by

contributions from quarks and gluons. As presented in equation (1.1), the spin of the nucleon can be decomposed as the sum of helicity and orbital angular momentum contributions of quarks and gluons in the nucleon

$$\frac{1}{2}\hbar = \frac{1}{2}\Delta\Sigma + \Delta G + L_q + L_g = J^q + J^g \quad , \tag{2.18}$$

where $J^{q,g}$ represent the total angular momenta of quarks and gluons in the nucleon. A promising way to access the total angular momenta J^q of quarks in the nucleon was pointed out in a work by Ji [9]. Therein, the second moments of the generalized parton distributions E and H can be related to form factors of the symmetric QCD energy momentum tensor

$$\int_{-1}^{1} dx\ x\ \ (H^q(x,\xi,t) + E^q(x,\xi,t)) = 2\,J^q(t) \quad . \tag{2.19}$$

In the case of zero momentum transfer ($t = 0$), J^q represents the total angular momentum carried by a quark of flavor q in the nucleon, i.e. the sum of spin and orbital angular momentum.

Relation (2.19) illustrates the importance of the generalized parton distribution E in the forward limit to access the contribution of the orbital angular momentum L_q of quarks to the nucleon spin. This forward limit is not accessible in DIS processes, as elucidated in Section 2.2.2, but can be investigated in hard exclusive reactions. From experimental results and by comparing to theoretical model-calculations for GPD E, using J^u and J^d as free parameters [28], there is a promising chance for pinning down the total angular momenta of quarks in the nucleon. Possible experimental ways to access generalized parton distributions are the exclusive production of a real photon in deeply virtual Compton scattering and the hard exclusive production of pseudo-scalar or vector mesons, which will both be presented in the following. An extended discussion about the potential of these two processes can be found in Chapter 4 of Ref. [28].

2.3 Deeply Virtual Compton Scattering

Deeply Virtual Compton Scattering (DVCS) is measured in exclusive production of real photons $lN \to \gamma lN$, or described in terms of amplitudes $\gamma^* N \to \gamma N$ (cf. Fig. 2.4). Apart from Compton scattering, the Bethe-Heitler process (BH), i.e. the initial or final state radiation of a single photon by the lepton, contributes to the same final state. Therefore, both mechanisms have to be added in the amplitude of the process $\gamma^* N \to \gamma N$.

The corresponding cross section is given by [28]:

$$\frac{d^4\sigma}{dQ^2\, dx_{Bj}\, dt\, d\Phi} \propto |T_{\mathrm{BH}} + T_{\mathrm{DVCS}}|^2 \quad , \tag{2.20}$$

where Φ denotes the azimuthal angle of the photon. T_{BH} and T_{DVCS} are the amplitudes of the Bethe-Heitler and the virtual Compton scattering process.

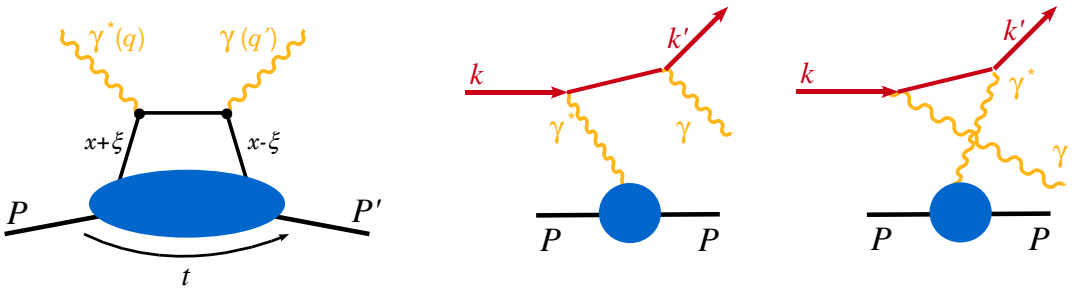

Figure 2.4: On the left-hand side, the handbag diagram, corresponding to deeply virtual Compton scattering on the level of amplitudes $\gamma^* N \rightarrow \gamma N$ is shown. The factorization into a hard leptonic and soft hadronic sub-process is visible. Generalized parton distributions investigated in this process are represented by the lower blob. The two graphs on the right-hand side depict the Bethe-Heitler process, where the final state photon γ is radiated from the initial or final lepton state. The structure information of the target nucleon in these processes is encoded in terms of usual parton distributions, as the initial and final nucleon states are equal.

Because information about generalized parton distributions is only contained in the virtual Compton scattering amplitude T_{DVCS}, the two contributions need to be disentangled. One possible experimental solution for this purpose is to use lepton beams of both charges, because the interference between the two processes changes sign when comparing the two scattering processes $l^+ N \rightarrow l^+ N\gamma$ and $l^- N \rightarrow l^- N\gamma$. Therefore, in the difference of cross sections $\sigma(l^+) - \sigma(l^-)$, the BH (whose amplitude is purely real) contribution drops out. Consequently, the cross section difference measures the real part of the BH-DVCS interference [29] and is therefore proportional to the *real* part of the DVCS amplitude T_{DVCS}

$$\sigma(l^+) - \sigma(l^-) \propto \mathrm{Re}\,[T_{BH} T^*_{DVCS}] \quad . \tag{2.21}$$

Another experimental possibility to disentangle the two contributions is, to measure the DVCS cross section in kinematic regions, where the DVCS contribution dominates over the BH contribution. This depends, for given values of x_{Bj}

and Q^2, mainly on the lepton beam energy E_l (cf. page 146–151 of Ref. [30]). In the case of dominance of the DVCS contribution, the cross section is essentially the square of the deeply virtual Compton scattering amplitude T_{DVCS}.

2.4 Hard Exclusive Meson Production

Generalized parton distributions can also be accessed through hard exclusive production of mesons. For longitudinally polarized photons, the factorization theorem for these processes was proven in Ref. [21]. The great advantage of these reactions is to study various aspects of GPDs, which are not accessible in Compton scattering, e.g. the detected final state can be used as a filter for spin, flavor, C-parity etc. of the removed and implanted quark (cf. black quark-line in Fig. 2.3). In addition, for hard exclusive vector meson production (e.g. ρ^0, ω, ϕ, ...) only the GPDs E and H and for pseudo-scalar meson production (e.g. $\pi^{0,\pm}$, $K^{0,\pi}$, ...) only $\tilde{E}$ and $\tilde{H}$ appear, while all of them contribute to the DVCS cross section. On the other hand, hard exclusive meson production is affected by larger theoretical uncertainties. Compared to the DVCS amplitude, an additional term, evoked by the presence of the meson, has to be taken into account for the amplitude of the process $lN \to lN\rho_L^0$ [17].

In the concept of s-channel helicity conservation (SCHC), the meson inherits its longitudinal polarization from the longitudinally polarized photon. Assuming the validity of SCHC, which is supported by experimental results [31, 32], the scattering process for hard exclusive meson production can also be expressed by:

$$\gamma_L^* N \to \rho_L^0 N \quad . \tag{2.22}$$

Similar to deeply virtual Compton scattering, the cross section for exclusive meson production can be expressed via these amplitudes [28]

$$\frac{d\sigma_L}{dt} \propto \frac{1}{2} \sum_{h_N} \sum_{h'_N} \left| \mathcal{M}_L(\lambda_{\mathrm{M}}, h_{N'}, h_N) \right|^2 \quad , \tag{2.23}$$

where $\mathcal{M}_L$ is the amplitude for the production of a longitudinally polarized meson with helicity λ_{M} and h_N, $h_{N'}$ are the helicities of the initial and final nucleon state.

Using the concept of SCHC the longitudinal photon cross section (2.23) for hard exclusive production of vector mesons can be accessed solely by measuring the angular distribution of the meson decay particles [33], i.e. without performing a Rosenbluth separation of longitudinal and transverse photon cross sections.

2.4.1 Transverse-Target Single-Spin Asymmetry

Beneath the longitudinal meson cross section, the transverse-target single-spin asymmetry $A_{\mathrm{UT}}(\phi_h - \phi_S)$ for a nucleon target polarized perpendicularly to the beam momentum involves only longitudinal amplitudes. In the following, this azimuthal asymmetry is discussed for the exclusive photo-production of a longitudinally polarized ρ^0 meson.

The azimuthal asymmetry is given by:

$$A_{\mathrm{UT}}(\phi_h - \phi_S) = \frac{d\sigma(\phi_h - \phi_S) - d\sigma(\phi_h - \phi_S + \pi)}{d\sigma(\phi_h - \phi_S) + d\sigma(\phi_h - \phi_S + \pi)} \tag{2.24}$$

where ϕ_h and ϕ_S are defined in the γN-system (GNS) as depicted in Figure 2.5. Therein ϕ_h is defined as the angle between the lepton scattering plane and the ρ^0 meson production plane and ϕ_S is the angle between the target spin vector and the scattering plane.

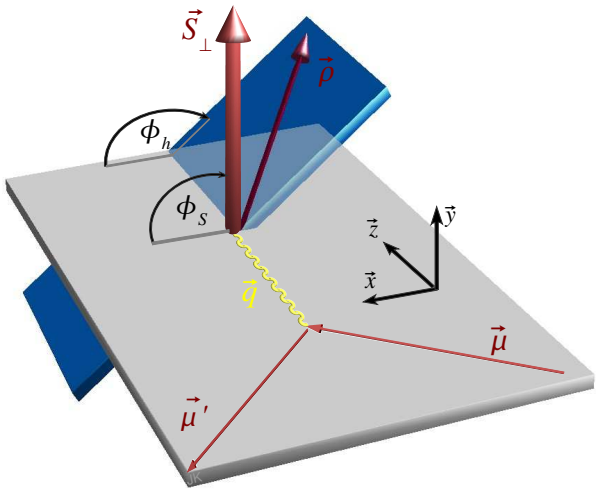

Figure 2.5: Definition of azimuthal angles ϕ_h and ϕ_S in the γN-system. The momentum vector of the virtual photon $\vec{q}$ defines the z axis and the x-z-plane is spanned by the momentum vectors of the incident and scattered muon. The y axis is defined in order to obtain a right-handed coordinate system. The azimuthal angle ϕ_S is defined as the angle between the lepton scattering plane (gray) and the spin vector $\vec{S}_\perp$ of the target, which is not necessarily perpendicular to the lepton scattering plane. The azimuthal angle ϕ_h is defined as the angle between the lepton scattering plane and the ρ^0 meson production plane (blue), where the latter is spanned by the momentum vectors of the virtual photon and of the ρ^0 meson.

The asymmetry $A_{\mathrm{UT}}(\phi_h - \phi_S)$ in equation (2.24) can also be expressed in terms of the amplitude $A_{\mathrm{UT}}^{\sin(\phi_h-\phi_S)}$ (cf. Ref. [34])

$$A_{\mathrm{UT}}(\phi_h - \phi_S) = A_{\mathrm{UT}}^{\sin(\phi_h-\phi_S)} \cdot \sin(\phi_h - \phi_S) \quad . \tag{2.25}$$

For the production of a longitudinally polarized ρ^0 meson, this amplitude is given by [28, 34]:

$$A_{\mathrm{UT}}^{\sin(\phi_h-\phi_S)} = -\frac{2|\Delta_{\mathrm{T}}|}{\pi} \frac{\mathrm{Im}(\mathcal{A}\mathcal{B}^*)/M_N}{(1-\xi^2)|\mathcal{A}|^2 - \left(\xi^2 + \frac{t}{4M_N^2}\right)|\mathcal{B}|^2 - 2\xi^2 \mathrm{Re}(\mathcal{A}\mathcal{B}^*)} \quad , \tag{2.26}$$

where M_N is the nucleon mass, $|\Delta_T| = \sqrt{-t(1-\xi^2) - 4\xi^2 M_N}$ the modulus of the perpendicular component of the momentum transfer $\Delta = \sqrt{t}$ and $\mathcal{A}$ and $\mathcal{B}$ represent amplitudes. These amplitudes can be expressed in terms of the generalized parton distributions E^q and H^q. For hard exclusive production of a longitudinally polarized ρ_L^0 meson on a transversely polarized *proton*[3] target P, the amplitudes $\mathcal{A}$ and $\mathcal{B}$ are given by [36, 37]:

$$\mathcal{A}_{\rho_L^0 P} = \int_{-1}^{1} dx \frac{1}{\sqrt{2}} (e_u H^u - e_d H^d) \left\{ \frac{1}{x - \xi + i\varepsilon} + \frac{1}{x - \xi - i\varepsilon} \right\} \quad , \tag{2.27}$$

$$\mathcal{B}_{\rho_L^0 P} = \int_{-1}^{1} dx \frac{1}{\sqrt{2}} (e_u E^u - e_d E^d) \left\{ \frac{1}{x - \xi + i\varepsilon} + \frac{1}{x - \xi - i\varepsilon} \right\} \quad , \tag{2.28}$$

where $H^{u,d}$ and $E^{u,d}$ are the generalized parton distributions of u and d quarks in the proton and $e_{u,d}$ the corresponding charges.

Equation (2.26) shows, that the amplitude $A_{\mathrm{UT}}^{\sin(\phi_h-\phi_S)}$ of the transverse-target single-spin asymmetry is proportional to the imaginary part of the *interference* of the two amplitudes $\mathcal{A}$ and $\mathcal{B}$, which contain the GPDs H and E respectively. Therefore $A_{\mathrm{UT}}^{\sin(\phi_h-\phi_S)}$ itself depends *linearly* on the GPD E. This linear dependence is contrary to the DVCS cross section or to the longitudinal meson cross section, where the GPD E appears kinematically power-suppressed and only in combinations with the generalized parton distribution H. Thus, in order to in-

[3] Similar equations can be derived for neutrons to completely describe the production of a longitudinally polarized ρ^0 on a deuteron target as it is used for this analysis. A discussion about GPDs in the deuteron can be found in Ref. [35].

crease the sensitivity to E in those observables, the value of the momentum transfer Δ has to be increased. However, the value of Δ should remain small, in comparison to the hard scale Q, in order to minimize higher twist effects (cf. discussion in Ref. [28]).

In this context, the amplitude $A_{\mathrm{UT}}^{\sin(\phi_h-\phi_S)}$ of the transverse-target single-spin asymmetry $A_{\mathrm{UT}}(\phi_h - \phi_S)$ provides a unique opportunity to extract the GPD E and thus, opens up the perspective of extracting the total angular momenta $J^{u,d}$ of quarks in the nucleon. This possibility originates from theoretical models for the generalized parton distribution E, using the total angular momenta $J^{u,d}$ as free parameters. Consequently, the extraction of information about the total angular momenta of quarks in the nucleon can be derived from comparison of results for $A_{\mathrm{UT}}^{\sin(\phi_h-\phi_S)}$ with theoretical predictions.

3 Experimental Setup

COMPASS[1] is a fixed target experiment, located at the M2 beam line of the **S**uper **P**roton **S**ynchrotron (SPS) at CERN[2]. Using a 160 GeV μ^+-beam, COMPASS investigated the spin structure of the nucleon with a polarized ^{6}LiD target during the years 2002-2004 and 2006. Therein 20% of the total beam time was dedicated to measurements on a target polarized perpendicularly to the beam momentum[3]. Therewith, COMPASS is currently the only experimental facility studying the transverse-target single-spin asymmetry $A_{\mathrm{UT}}(\phi_h - \phi_S)$ on a transversely polarized deuteron target.

Experimental investigations on a transversely polarized *proton* target started recently. The combination of present results and results from these ongoing measurements, will lead to the extraction of structure information of the neutron.

The purpose of this chapter is to describe the experimental setup in Section 3.1 and 3.2. Because measurements with the transversely polarized deuteron target were performed only during the years 2002-2004, the description of the experimental setup is limited to this period. In addition, the software used for the analysis of the recorded data is presented in Section 3.3. An extended review of the COMPASS experiment and specific technical details can be found in Ref. [39].

3.1 Beam And Target

3.1.1 The 160 GeV μ^+-Beam

The 160 GeV μ^+-beam is a tertiary beam, originating from protons, accelerated in the SPS. These protons are extracted into the M2 beam line (cf. Fig. 3.1), where the secondary beam, consisting mainly of pions and kaons, is produced on a beryllium production target. Via a setup of dipole magnets and scrapers, pions and kaons in a specific momentum interval are selected. Most of these secondary beam particles decay within a very short characteristic lifetime into muons. After absorption of remaining pions and kaons in a hadron absorber and a second

[1] **CO**mmon **M**uon and **P**roton **A**pparatus for **S**tructure and **S**pectropy

[2] European organization for nuclear research

[3] An overview of the extensive physics program of COMPASS can be found in Ref. [38] and Ref. [30], where in the latter future investigations are outlined.

momentum selection, the μ^+-beam is focused onto the polarized COMPASS target. The momenta of beam muons are measured in the Beam Momentum Station (BMS), which consists of several hodoscope planes. A detailed review about operation and setup of the BMS can be found in Ref. [40].

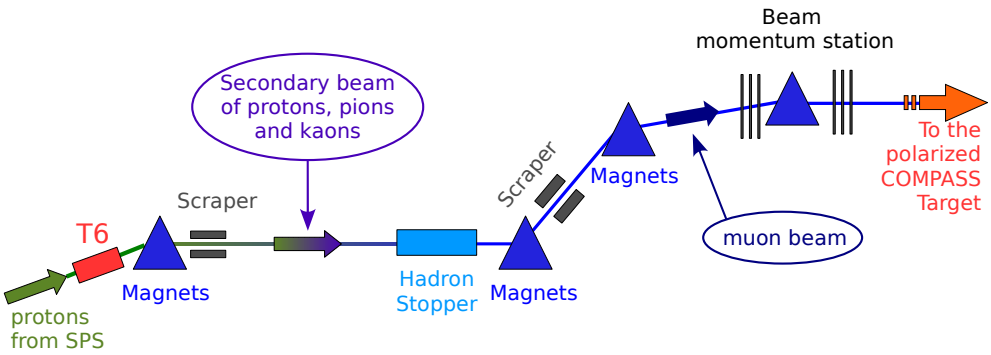

Figure 3.1: Schematic of the M2 beam line. The primary beam of protons is extracted from the SPS into the M2 beamline, where the secondary beam, consisting of pions and kaons, is produced at the T6 beryllium production target. These pions and kaons decay into muons. The hadron contamination in this tertiary beam is filtered out by the hadron stopper. Via bending magnets and scrapers the muon beam is momentum selected and focused on the polarized COMPASS target. In the beam momentum station, the momenta of beam particles are measured.

3.1.2 The Polarized ^{6}LiD Target

To achieve high luminosities, the COMPASS experiment uses a thick solid state target. The ^{6}LiD target material is contained in two oppositely polarized cylindrical target cells (cf. Fig. 3.2), surrounded by a complex setup of a cryostat and a superconducting solenoid and dipole magnet. This setup serves for polarizing the target nuclei using the method of dynamic nuclear polarization [41].

The advantage of having two target cells with opposite polarizations is that measurements of cross section asymmetries are independent of the muon flux and of time-dependent detector-acceptance effects (cf. Chapter 5). For longitudinal polarization of the target nuclei, with respect to the beam momentum, a superconducting solenoid is used. In addition, for adiabatically reversal of the target spins, a well-tuned ramp-up and ramp-down procedure for the solenoid and the dipole magnet is used. Moreover, this procedure serves to hold a transverse polarization of the target nuclei with respect to the beam direction.

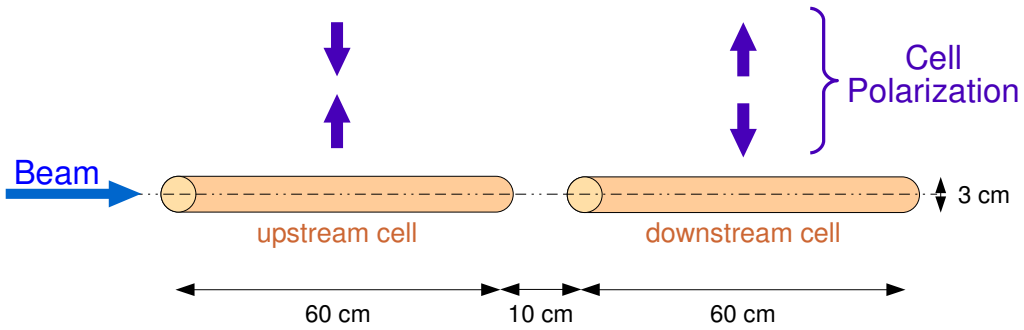

Figure 3.2: Schematic of the two polarized ^{6}LiD target cells. The upper blue arrows indicate the possible polarizations of the target nuclei during data-recording with a transversely polarized target.

3.2 The COMPASS Apparatus

The COMPASS apparatus, as depicted in Figure 3.3, is a two stage spectrometer, equipped with two spectrometer magnets called SM1 and SM2. For measurements of particle momenta, particle identification and calorimetry, several detectors are used as explained in the following.

3.2.1 Tracking Detectors

In both stages of the apparatus, tracking detectors are used to determine the momenta of charged particles. These can be divided into three groups: detectors for very small, small and large scattering angles. Due to the very high track densities in the central region, detector types capable of very high rates and excellent time resolution are needed. For this purpose, COMPASS uses silicon and scintillating fiber detectors for tracking of particles scattered at very small angles. Gas detectors like **G**as **E**lectron **M**ulipliers (GEMs) and **Micro Me**sh **ga**s detectors (MicroMegas) with an excellent spatial resolution serve for the detection of charged particles scattered at intermediate angles up to a distance of about 30–40 cm from the beam direction. Finally, to cover the remaining area, charged particles scattered at large angles are detected by **M**ulti-**W**ire **P**roportional **C**hambers (MWPCs), **STRAW** tube detectors (STRAWs) and **D**rift **C**hambers (DCs).

To avoid detector occupancies exceeding their maximal rate capability, the small and large area trackers are designed with holes or dead zones in their central regions.

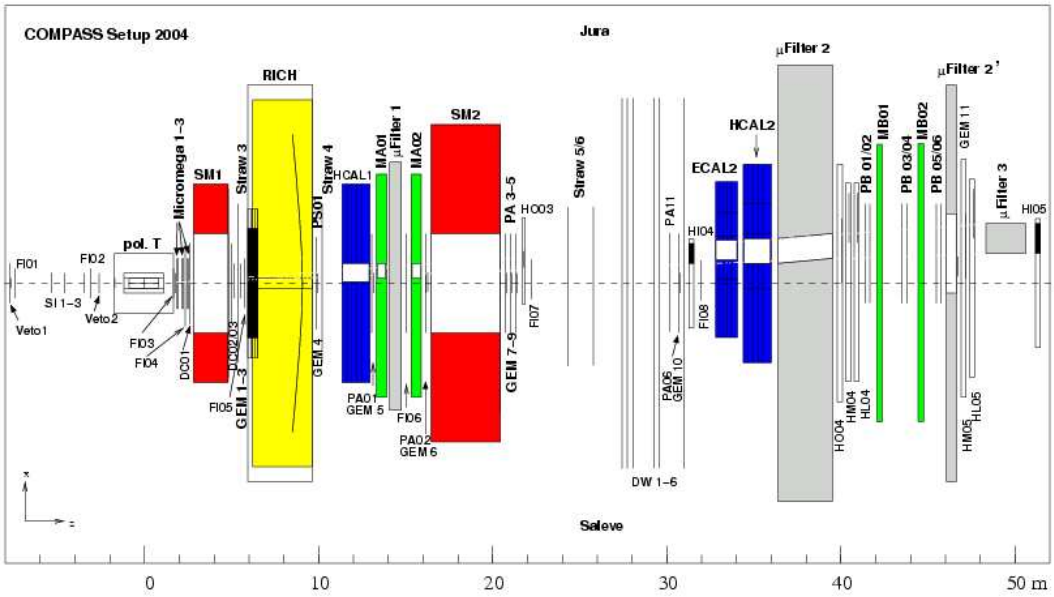

Figure 3.3: Top view of the COMPASS apparatus during the 2004 data-recording period [39]. The muon beam, entering from the left-hand side, is detected by Scintillating Fiber (FI) and Silicon (SI) detectors, located upstream of the polarized ^{6}LiD target. The remnants of reactions are detected in the two stages of the apparatus. Particles with lower momenta and therefore large scattering angles, are detected in the first stage, while, in the second stage, particles with higher momenta and small scattering angles are detected. Both spectrometer stages are equipped with various tracking detectors (FIs, GEMs, MicroMegas, STRAWs and DCs), calorimeters (HCAL1,2 and ECAL2) and detectors for particle identification (Muon Wall detectors (MAs), μFilters and the RICH). In addition, the trigger hodoscopes (Vetos and HOs) are depicted. The dead zones mentioned, and especially the holes, can be seen very clearly, e.g. in the calorimeters or in the second muon filter (μFilter2).

3.2.2 Particle Identification

The particle identification (PID) in the COMPASS experiment is organized in two steps. In the first step, a distinction between muons and hadrons is achieved by their different characteristic behavior in penetrating matter, while in the second step, different types of charged hadrons (e.g. pions and kaons) can be separated by using information from a **R**ing **I**maging **CH**erenkov detector (RICH).

In order to avoid absorption of particles scattered at very small angles in the first stage of the apparatus or interactions of beam particles, the calorimeters and muon wall detectors (cf. Fig. 3.3 and the following sections) are designed with physical holes in their central regions.

Muon Wall Detectors

The majority of hadrons are absorbed in the hadronic calorimeters (cf. Sec. 3.2.3) or in the muon filters, i.e. thick walls of concrete or iron, placed behind the calorimeters. On the contrary, muons do not obey the strong interaction. Thus, they can penetrate thick layers of material without being absorbed. Particles passing the upper absorbers are detected by Muon Wall detectors (MA01 and MA02), built as Iarocci or drift tube detectors, which are located directly in front of and behind the muon filter μFilter1.

Ring Imaging Cherenkov Detector

For the separation of charged particle types above a particle-specific momentum threshold, COMPASS uses a **R**ing **I**maging **CH**erenkov detector (RICH), placed in the first stage of the apparatus. The radiator gas used for producing Cherenkov photons is C_4F_{10}. Until the end of 2004 photon-detection was performed by multi-wire proportional chambers, equipped with CsI photo cathodes. More information about the RICH-1 detector can be found in Ref. [42].

3.2.3 Calorimetry

The energy of hadrons is measured in form of their energy deposit in the hadronic calorimeters (HCAL1 and HCAL2). This information can also be used to distinguish between hadrons and muons, because the latter deposit less energy in the HCALs. By determining the center of deposited energy and additional tracking information, the energy measured can be assigned to a certain particle. The energy of electrons and photons can be determined in an electromagnetic calorimeter ECAL2, located upstream of the hadronic calorimeter HCAL1. During the data-recording periods in 2002, a lead wall of about the same size as ECAL2 was used, serving as an electron and photon absorber, prior to final installation of ECAL2.

3.2.4 The Trigger System

The COMPASS experiment operates with high beam intensities and a thick solid state target. This enables high luminosities to be achieved, leading to high event rates. The necessary pre-selection of desired events at the hardware level is performed by the trigger system [43], depicted in Figure 3.4. For the detection of scattered muons, dedicated hodoscopes are installed, which are grouped to the so-called *inner*, *ladder*, *middle* and *outer* trigger. This setup of muon triggers permits the separation of events in different kinematic ranges of Q^2 and ν, by selecting events with a certain deflection angle of the scattered muon. In addition

to the muon triggers, detector information from the hadronic calorimeters can be used to trigger on events with a hadron candidate. Veto hodoscopes, placed in front of the target, prevent triggering on muons from the beam halo instead of events with a scattered muon.

For the trigger signal generated, the combined information from the muon, calorimeter and veto triggers are used. This signal determines whether the detector information is read out or not.

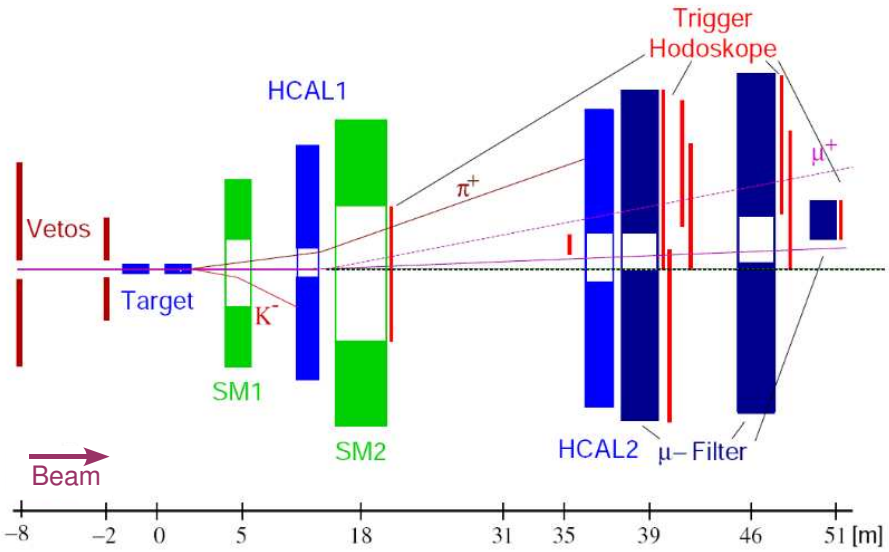

Figure 3.4: Schematic of the trigger setup [43]. The information from dedicated veto hodoscopes (upstream of the target) impede a trigger signal initiated by a beam particle. The energy deposit information from the hadronic calorimeter HCAL1 can be used to trigger the readout of detectors for events with hadron candidates. In addition, the muon trigger hodoscopes (depicted in red) are used to select specific kinematic ranges of Q^2 and ν.

3.2.5 The Data Acquisition System

The Data Acquisition (DAQ) System [44, 45], depicted in Figure 3.5, needs to fulfill the requirements imposed by high event rates. Therefore, the detector information is digitized right at the detector on *front-end* cards or dedicated Mezzanine cards and transferred to the **C**OMPASS **A**ccumulate, **T**ransfer and **C**ontrol **H**ardware (CATCH) [46, 47] or **GE**M and **Si**licon **C**ontrol and **A**quisition [48] (GESiCA) modules. If a trigger signal for these data arrives via optical fibers

from the **T**rigger **C**ontrol **S**ystem (TCS) [48, 49], the data are transferred by optical links to the DAQ barrack. On so-called readout-buffer PCs the data are temporarily stored, before being processed in an event builder farm. In the event-building procedure, detector information are combined belonging to one event, i.e. when the read-out of detectors was triggered, e.g. by the appearance of a scattered muon in a certain kinematic range of Q^2. Finally, the data are transferred via a dedicated network to the **C**entral **D**ata **R**ecording (CDR).

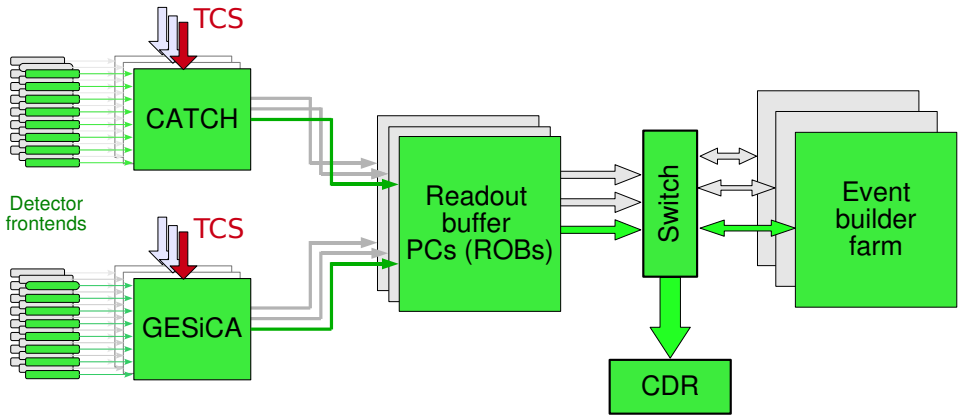

Figure 3.5: COMPASS data acquisition system. Digitized detector information is transferred to CATCH and for some detectors GESiCA modules. In case of a trigger signal from the trigger control system (TCS), the data are sent to readout buffer PCs. Via a GigaBit switch, the data are further transferred to the event builder farm, where the streams of information from one event are combined. Finally, the data are stored in the central data recording (CDR).

The data recorded are organized in so-called runs. These are grouped together in periods consisting of data from measurements with one target polarization configuration (cf. Fig. 3.2). Once detector calibrations and alignment information are ready, the raw data can be further processed and analyzed.

3.3 Reconstruction and Analysis Software

The **CO**MPASS **R**econstruction and **A**na**L**ysis Framework (CORAL) [50] is used for reconstructing the raw data. During this procedure, particle tracks and vertices are reconstructed and detector information, e.g. from the calorimeters or the muon trigger hodoscopes, are processed. After this first step, the data are stored in **D**ata **S**ummary **T**ape (DST) files, which can be read again by CORAL for

further analyses. In addition, events which contain at least one vertex are stored in **m**ini DST (mDST) files, which can be analyzed using a dedicated software environment called **PH**ysics **A**nalysis **S**oftware **T**ools (PHAST) [51]. On this level, the selection of events for particular analyses and the calculation of physics quantities can be performed.

The results obtained in this thesis originate from specially-written software, which was implemented within the framework of PHAST and ROOT [52], where the latter is an analysis framework for high-energy physics data provided by CERN.

4 Reconstruction of Exclusively Produced ρ^0 Mesons

For extraction of the amplitude $A_{\mathrm{UT}}^{\sin(\phi_h-\phi_S)}$ of the transverse-target single-spin asymmetry a data sample is needed consisting of events with exclusively produced ρ^0 mesons. The content of this chapter is therefore a detailed description of the event selection performed (Section 4.1 – 4.5). Finally, the characteristics of the data sample obtained for the full statistics are presented in Section 4.6.

In this analysis a sample of COMPASS data recorded during the years 2002-2004 with the transverse-target spin configuration is used as the initial data sample. It consists of events with at least one primary vertex, i.e. a vertex related to the track of the beam particle and a well-defined scattered muon. Moreover, at least one additional charged track outgoing from this primary vertex is required[1]. Finally the deep inelastic scattering region is selected by restriction on the photon virtuality $Q^2 > 1$ $(\mathrm{GeV/c})^2$.

4.1 Data Quality

The basic criterion for the extraction of physical information is successful operation of the experimental setup. Since fluctuations are not entirely avoidable the recorded data is checked to ensure a good performance of the apparatus and thus the needed quality of data. The description of the monitoring procedure and the rejection criteria for unstable runs is presented in this Section. An extended review of this monitoring procedure can be found in Ref. [53].

In general, the stability is checked for several parameters by comparison with average values in a period or a sub-period. This procedure can be divided roughly into four blocks as shown schematically in Table 4.1. Therein, the first block describes the rejection criteria for runs due to detector failures, while the second focuses on the reconstruction stability. In the third block the global performance of the apparatus is monitored by reconstructing K_0 events. This method is chosen,

[1] This requirement is motivated by analyses of asymmetries appearing in semi-inclusive production of hadrons.

because therein well-known physical quantities appear [54]. Finally, a sub-sample[2] is used to validate the stability of primary vertex coordinates, several kinematic variables and azimuthal angles.

Table 4.1: Schematic overview of data stability monitoring used for data recorded with the transverse-target spin configuration.

Block1	Detectors' profiles
Block2	Number of tracks per event in total and for different zones(∗) Number of tracks with momentum per event Number of primary vertices per event Number of secondary vertices per event Total number of clusters per event Total number of clusters per plane
	(∗) upstream the target, upstream SM1, between SM1 and SM2, between SM2 and MF1 and downstream MF1
Block3	K_0 mass shift vs. run number K_0 mass resolution vs. run number Number of reconstructed K_0 per primary vertex vs. run number
Block4	Stability vs. Time Period for: X_{PV}^{upCell}, Y_{PV}^{upCell}, $X_{PV}^{downCell}$, $Y_{PV}^{downCell}$, x_{Bj}, Q^2, y, $\Phi_{LAB}^{\mu'}$, Φ_{Breit}^{h}, Φ_{LAB}^{h}, p_h^{tot}, $E_{HCAL1/2}$

4.2 The μ^+ beam and the scattered muon μ'

After general checks on the stability of data, particular constraints can be applied. First of all, a crossing of the beam particle through the target region and equal beam particle fluxes in both target cells are ensured by extrapolation of the incident beam particle track to the upstream end of the first (upstream) target cell and to the downstream end of the second (downstream) target cell. For these two z coordinates, the intersection points of the beam track with the target cylinders[3] are calculated. Events are rejected if the radial distance of one of these intersection points is larger than 1.3 cm.

[2] On this sub-sample, the standard kinematic requirements for the analysis of the Collins and Sivers asymmetry [55] are applied.

[3] The magnetic field used for the polarization of the target cells causes displacements of the target cylinders, which were taken into account for the analysis. Numerical values for these corrections can be found in Ref. [56].

Each particle track during reconstruction is derived from the tracking detector data by using a Kalman fit. The same holds for the determination of vertex coordinates. Therefore, the quality of the data sample can be increased by rejecting insufficiently reconstructed tracks and vertices with a reduced $\chi^2_{\text{red}} > 10$. Additionally, the physical reaction, which is ideally related to the occurrence of a primary vertex, must have taken place in one of the two target cells. Occasionally, there are several primary vertices in one event. In this case the *best* primary vertex is selected. This denotes the primary vertex with the largest number of associated tracks or, in case of number-equality, the vertex with the best χ^2 of the fit.

To ensure the reaction took place in one of the two target cylinders, the radial distance of the primary vertex must be smaller than 1.3 cm and its z coordinate must lie in the range of one of the two target cells

$$-100 \text{ cm} < z < -40 \text{ cm} \quad \text{or} \quad -30 \text{ cm} < z < 30 \text{ cm} \ . \tag{4.1}$$

The spatial distributions of primary vertices are depicted in Figure 4.1, where in the right graph a clear separation of the two target cells can be recognized.

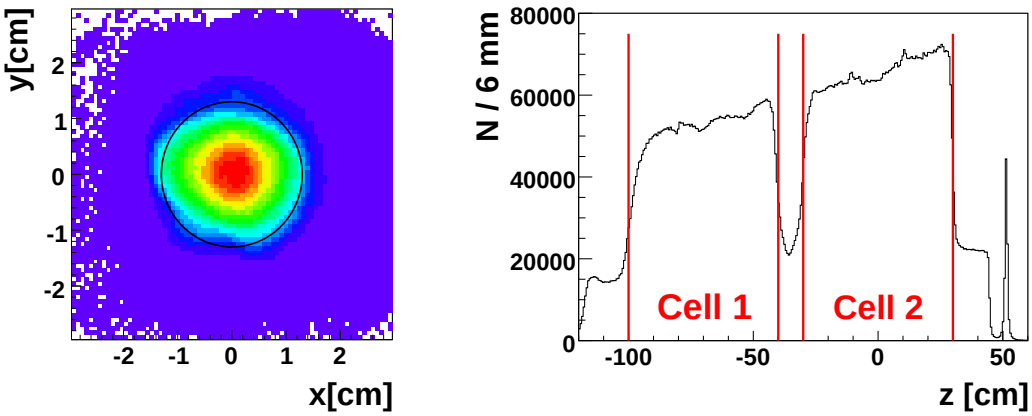

Figure 4.1: Spatial distributions of (best) primary vertices for the 2003 data are shown before applying any constraints. The left graph shows the plane perpendicular to the beam axis with a black circle superimposed, indicating the permitted area. On the right-hand side, the distribution in z-direction is shown. The ends of the target cells are indicated by red lines.

In closer inspection of particles outgoing from the primary vertex, the first particle considered is the scattered muon μ'. To distinguish between the scattered beam particle and other particles produced in the reaction, two methods are used.

One is based on a CORAL routine, wherein the scattered muon is *tagged* as such during reconstruction. For the other method, an algorithm is used to recover a scattered beam particle among the particles outgoing from the primary vertex. For this method, the hit information of the two Muon Wall detectors MA01 and MA02 are inspected for all particle tracks outgoing, except for the track associated to the tagged μ'. An indication for an untagged scattered muon is the appearance of more than three hits in the first and more than five hits in the second muon wall associated with a particle track. If these tracks exhibit also a reduced $\chi^2_{\text{red}} < 10$ and a measured penetration length $nX/X_0 > 30$, they are marked as *recovered* muons.

The calculated penetration length nX/X_0 quantifies the amount nX of detector material passed normalized to the particle-specific radiation length X_0 in these materials. For the calculation of the radiation length X_0, particle-specific interaction processes within matter, e.g. electromagnetic interactions in the calorimeters, have to be taken into account. The amount of matter passed by the particle is obtained using a material map of COMGEANT [57].

Finally, only events containing exactly one scattered muon (either *tagged* or *recovered*) are subjected to the further analysis. To ensure a well-defined track and that the particle crossed a sufficient amount of detector material, as it is characteristic for minimal ionizing particles, the finally selected scattered muon track is checked again for a reduced $\chi^2_{\text{red}} < 10$ and $nX/X_0 > 30$. This obvious duplication of requirements is needed for a *tagged* scattered muon.

4.3 Cuts on inclusive scattering variables

The inclusive scattering variables are calculated using the tracks associated with the incident and the scattered muon. For ensuring hard scattering processes, the photon virtuality is restricted to

$$Q^2 > 1.0 \ (\text{GeV/c})^2 \quad . \tag{4.2}$$

By applying a cut on the invariant mass squared of the final hadronic state

$$W^2 = (q + P)^2 > 25 \ \text{GeV}^2/\text{c}^4 \quad , \tag{4.3}$$

where q and P denote the four-momenta of the virtual photon and of the target nucleon, the region of hadron resonances is excluded. Another kinematic variable taken into account is the relative energy transfer y, defined via the four-momenta

P of the target nucleon, q of the virtual photon and k of the beam particle

$$y = \frac{P \cdot q}{P \cdot k} \overset{Lab}{=} \frac{\nu}{E_\mu} \quad , \tag{4.4}$$

where the second relation is valid in the laboratory system.

To avoid events in the kinematic region of elastic scattering, the energy loss of the beam muon is required to exceed a minimal value. Furthermore the energy of the scattered muon should be large enough to avoid reactions dominated by radiative corrections. These two requirements are implemented by the restriction

$$0.1 < y < 0.9 \quad , \tag{4.5}$$

on the range of the energy fraction y in the data sample.

4.4 Hadrons

Observation of exclusive processes generally means that every final state particle is detected. For the present purpose, only events with a fixed number of final state particles are taken into account. This would imply, for the exclusive production of a ρ^0 meson, a restriction to two particles outgoing from the primary vertex, the scattered muon and the produced ρ^0 meson. However, the experimental vertex resolution is insufficient for the very short characteristic lifetime of the ρ^0 meson of about $4.4 \cdot 10^{-24}$ s.

Instead, the ρ^0 meson is reconstructed via its decay particles. Because the branching ratio for the process $\rho^0 \to \pi^+\pi^-$ is almost 100% [58], only events with three particles outgoing from the primary vertex are taken for further analysis, particularly those events with a scattered muon and two particles of opposite charge.

As for determination of the scattered muon (cf. Section 4.2), the associated particle tracks need to be well-defined. This is ensured by requiring for each of them $\chi^2_{\text{red}} < 10$. Since the reconstruction of tracks in the so-called fringe field[4] is difficult and does not work entirely satisfactorily, events with tracks ending in this region are rejected.

[4]The term *fringe field* denotes the region between the polarized ^{6}LiD target and the magnet SM1 (cf. Fig. 3.3). The difficulty of track-reconstruction arises from determination of the effective magnetic field in this region.

In the following, the particles produced are assumed to be charged π mesons. This necessarily implies a verification of their hadronic nature. As hadrons are strong interacting particles, this can be done by restricting their measured penetration length to $nX/X_0 < 10$. Additionally, events are rejected in which one of the π candidates produces a detector hit behind the second muon filter. In such cases, correct distinction between muons and hadrons is difficult, because the hadron could have escaped the cut on the penetration length. This is possible for particles crossing the apparatus close to the beam region, i.e. through the holes of the calorimeters and muon filters (cf. Section 3.2.1).

For the same reason, the π^+ candidate is occasionally mistaken for the scattered muon and vice versa. In this case, the high energetic meson crosses the apparatus close to the beam region and therefore has a large penetration length assigned to it. On the other hand, the scattered muon track might lie outside of the detector acceptance, since its track exhibits a large angle with respect to the beam. One problem resulting from this misidentification is, e.g. miscalculation of the inclusive scattering variables (cf. Section 4.3).

Based on geometrical considerations, a method for elimination of such scenarios was introduced in Ref. [59]. According to this method, the positively charged hadron track is extrapolated to the downstream end of the apparatus ($z = 5000$ cm). From this procedure, the coordinates x_e and y_e can be extracted, denoting the spatial coordinates of track intersection with the plane perpendicular to the beam at this location. Depending on the last observed detector hit of the π^+ candidate, a geometrical cut is applied. Particle tracks ending in the large angle stage of the apparatus ($z_\mathrm{last} < 2000$ cm) need to fulfill the requirement

$$\sqrt{(x_\mathrm{e} - 45\ \mathrm{cm})^2 + y_\mathrm{e}^2} > 10\ \mathrm{cm} \quad , \tag{4.6}$$

whereas those ending in the small angle stage of the spectrometer need to meet the conditions

$$\sqrt{(x_\mathrm{e} - 35\ \mathrm{cm})^2 + y_\mathrm{e}^2} > 15\ \mathrm{cm} \qquad \text{or} \tag{4.7}$$

$$|y_\mathrm{e}| > 3\ \mathrm{cm} \quad \text{and} \quad |x_\mathrm{e} - 55\ \mathrm{cm}| > 13\ \mathrm{cm} \quad .$$

Events with positively charged tracks not meeting these requirements are removed from the data sample. For illustration the calculated spatial distributions of the π^+ candidate track can be found in Figure 4.2.

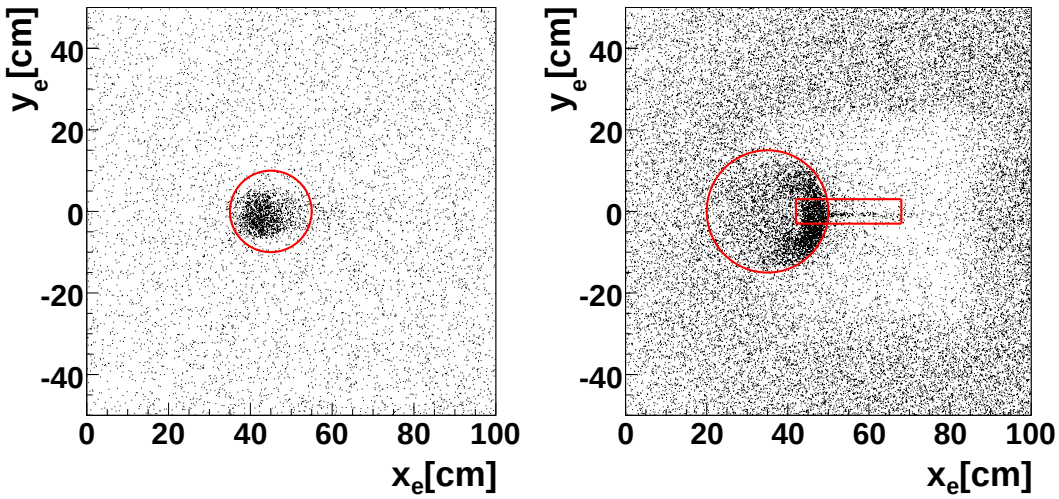

Figure 4.2: Spatial distribution of extrapolated track coordinates in the plane perpendicular to the beam direction at $z = 5000$ cm for the 2003 data. The left-hand graph displays the distribution of tracks ending in the large angle stage of the apparatus. On the right-hand side, the spatial distribution for tracks ending in the small angle stage are shown. The superimposed red box and circles indicate geometrically excluded regions.

Finally, the hadronic calorimeters are scanned for clusters of deposited energy. For particles with associated clusters in both hadronic calorimeters the whole event is rejected. Such tracks probably result from inaccurate reconstruction, as the occurrence of associated clusters in both hadronic calorimeters is geometrically prohibited by the experimental setup.

4.5 Exclusive ρ^0 sample

As already mentioned, the final sample should be enhanced with exclusively produced ρ^0 mesons. However, the sample derived from the event selection procedures described above still contains other particles (e.g. ϕ mesons decaying into two K mesons of opposite charge) and non-exclusive background. To minimize the non-exclusive background a small missing energy

$$E_{\text{miss}} = \frac{M_{P'}^2 - M_P^2}{2 \cdot M_P} = \frac{(P + q - \rho)^2 - M_P^2}{2 \cdot M_P} \tag{4.8}$$

is required. In principle this quantity is determined using the target particle mass M_P and the mass of the recoiling target particle $M_{P'}$. Unfortunately, recoil detection is impossible, due to the huge amount of material around the target cells,

introduced by the cryostat and the magnets. Hence, the mass $M_{P'}$, respectively the four-momentum vector of the recoiling target particle, is reconstructed using four-momentum conservation. For this purpose the four-momentum vectors P of the target particle, q of the virtual photon and ρ of the produced ρ^0 meson are used. As elucidated in Section 4.4 the ρ^0 meson is reconstructed via its decay particles, to which the pion mass $M_\pi = 139.6$ MeV [58] is assigned. Thus, the calculation of the mass $M_{P'}$ implies a significantly lower resolution for the missing energy E_{miss} of about 1 GeV [60]. Consequently the chosen range for this quantity is

$$-2.5 \text{ GeV} < E_{\text{miss}} < 2.5 \text{ GeV} \tag{4.9}$$

in the final data sample. In Figure 4.3, the distribution of the missing energy is shown before applying the cut on the allowed range.

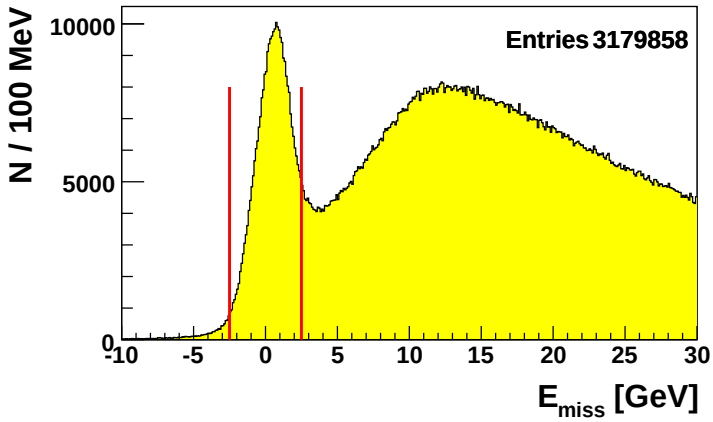

Figure 4.3: Distribution of the missing energy E_{miss} for the full 2002-2004 data sample, before applying the cut on the permitted range. For illustration the red lines indicate the restrictions for the final data sample.

For the extraction of azimuthal asymmetries, a reliable definition of the angle between the lepton scattering plane and the hadron production plane (cf. Section 2.4.1) is necessary. This is ensured by a lower limit for the quantity p_{T}, which is defined in the γN-system as the transverse component of the momentum vector of the ρ^0 meson with respect to the direction of the virtual photon. Further reduction of contributions from non-exclusive background events, an be achieved by setting an upper limit for p_{T}^2 [61, 62]. For illustration, distributions of the missing energy in different ranges of p_{T} are shown in Figure 4.4. With

both requirements, the range

$$0.01\ (\mathrm{GeV/c})^2\ <\ p_{\mathrm{T}}^2\ <\ 0.5\ (\mathrm{GeV/c})^2\ . \tag{4.10}$$

was chosen for events in the final data sample.

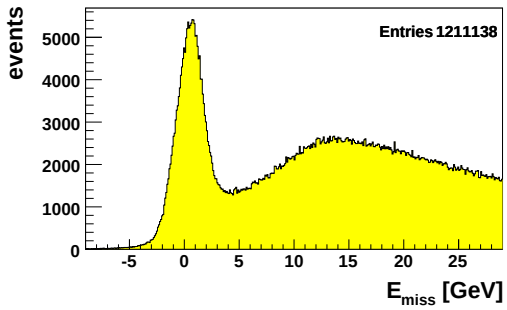

(a) Distribution of the missing energy with the restriction $p_{\mathrm{T}} < 0.3$ (GeV/c)

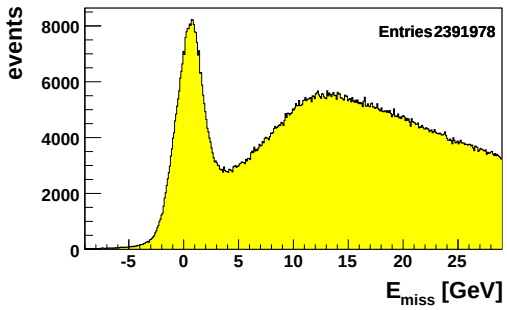

(b) Distribution of the missing energy with the restriction $p_{\mathrm{T}} < 0.5$ (GeV/c)

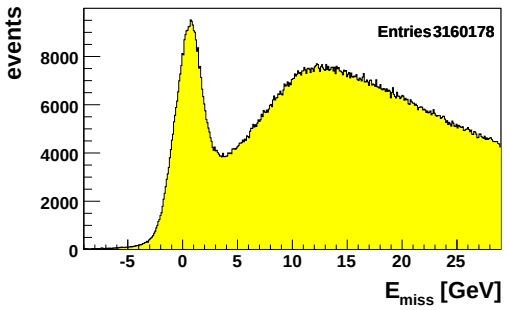

(c) Distribution of the missing energy with the restriction $p_{\mathrm{T}} < 0.7$ (GeV/c)

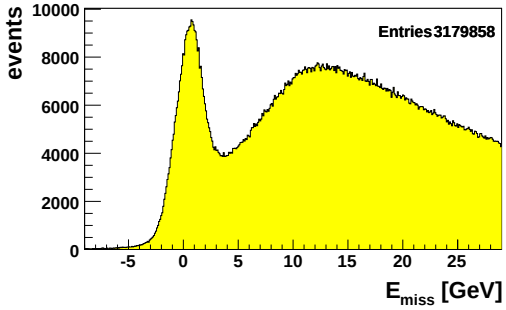

(d) Distribution of the missing energy without restriction on p_{T}

Figure 4.4: Distributions of the missing energy in different ranges of p_{T} for the full 2002-2004 statistics before applying restrictions on E_{miss}. The allowed ranges of the perpendicular momentum component p_{T} are given in the captions of the graphs. The reduction of non-exclusive background by restrictions on p_{T} can be seen in these distributions.

Finally, the invariant mass distribution, depicted in Figure 4.5, shows clearly the ρ^0 mass peak at the expected value of about $M_\rho = 775.5$ MeV [58]. However, contributions of other particles can be recognized, e.g. a ϕ meson peak located at an incorrect mass value due to the "false" assignment of masses to the decay particles. Requiring an invariant mass $M_{\pi\pi}$ in the range

$$-0.3\ \mathrm{GeV/c}^2\ <\ (M_\rho - M_{\pi\pi})\ <\ 0.3\ \mathrm{GeV/c}^2 \tag{4.11}$$

reduces significantly the contributions of other exclusively produced particles in the data sample.

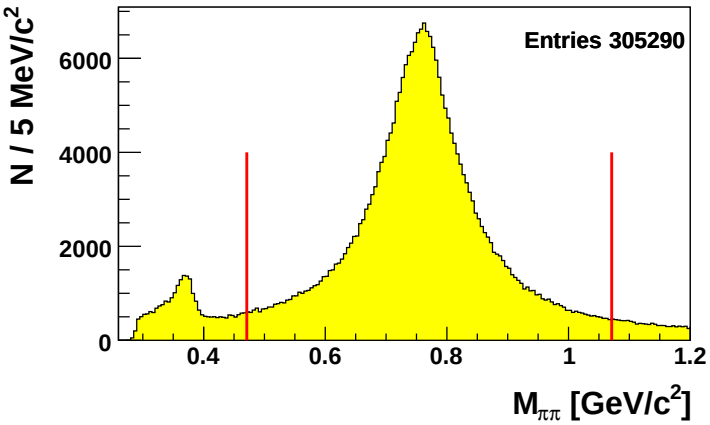

Figure 4.5: Invariant mass spectrum $M_{\pi^+\pi^-}$ for the full 2002-2004 data sample, before applying the cut on the permitted range. The superimposed red lines indicate the restrictions for the final data sample.

4.6 Final data sample

After the detailed description of the event selection performed in this analysis, this section is dedicated to the characteristics of the final data sample.

From the 2002-2004 COMPASS data with a transverse-target spin configuration 270,163 events are selected, which is about 0.5% of events in the initial data sample. The event yields per year of data-recording are listed in Table 4.2.

The finally selected sample of events contains an enhanced fraction of hard exclusively produced ρ^0 mesons. From the kinematics of these events, the amplitude $A_{\mathrm{UT}}^{\sin(\phi_h-\phi_S)}$ can be extracted (cf. Chapter 5). The kinematic variables of special interest for this purpose are the Bjorken variable x_{Bj}, the photon virtuality Q^2, the transverse momentum component p_{T} and t'. Therein t' is calculated as the difference of the Mandelstam variable t and its minimal kinematically allowed value t_{min} (cf. pages 321–324 of Ref. [58])

$$t' = t - t_{\mathrm{min}} = -2\,|\vec{\rho}|\,|\vec{q}|\,(1-\cos(\theta)) \quad . \tag{4.12}$$

For the calculation of t', the momentum vectors $\vec{\rho}$ and $\vec{q}$ of the ρ^0 meson and the

Table 4.2: Event yield per year of data-recording obtained after the selection of events.

Year	2002	2003	2004	**TOTAL**
# Events	39,583	84,543	146,037	**270,163**

virtual photon in the γN-system and the angle θ between these vectors are used. The minimal kinematically allowed value $t_{\min}$ corresponds to scattering processes, where the value for the angle between the initial and final state nucleon is $\theta = 0$ or $\theta = \pi$ in the γN-system.

Distributions of the kinematic variables x_{Bj}, Q^2, p_{T}^2 t', y and W are presented in Figures 4.6 – 4.8. The corresponding mean values of these variables in the final data sample are listed in Table 4.3.

Table 4.3: Mean values of the kinematic variables in the final sample selected from the 2002-2004 data.

$\langle\, x_{Bj} \,\rangle$	=	0.030	
$\langle\, Q^2 \,\rangle$	=	1.93	$(\mathrm{GeV/c})^2$
$\langle\, p_{\mathrm{T}}^2 \,\rangle$	=	0.118	$(\mathrm{GeV/c})^2$
$\langle\, -t' \,\rangle$	=	0.126	$(\mathrm{GeV/c})^2$
$\langle\, W \,\rangle$	=	8.71	$\mathrm{GeV/c^2}$
$\langle\, y \,\rangle$	=	0.279	

In addition to one-dimensional distributions, the two-dimensional distribution of Q^2 vs x_{Bj} is shown in Figure 4.6. Furthermore, the two-dimensional distribution of $-t'$ vs p_{T}^2 is presented in Figure 4.7. Therein a pronounced correlation between $-t'$ and p_{T}^2 at small values can be seen. This strong correlation becomes slightly weaker for larger values, which might be a hint for remaining non-exclusive background contributions in the final data sample (cf. Ref. [61]), because the calculation of t' in the form of equation 4.12 is only valid for exclusive processes. The remaining contribution of non-exclusive background events is quantified and discussed in Section 6.4.

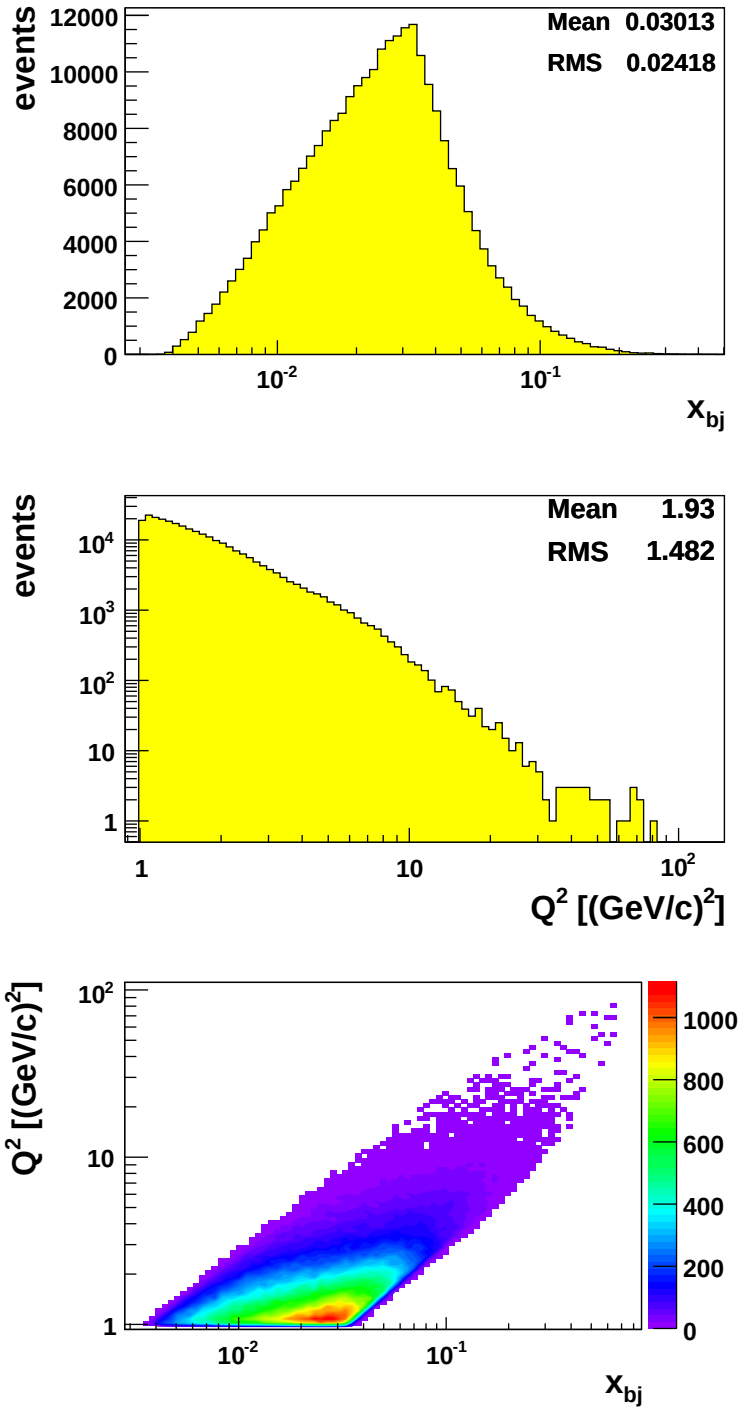

Figure 4.6: Distributions of the kinematic variables x_{Bj} and Q^2 for the final data sample. In addition, the two-dimensional plot for the upper variables is presented. Therein, the highest contributions in the final data sample events with $x_{Bj} \simeq 0.03$ and $Q^2 \simeq 1.1(\mathrm{GeV/c})^2$.

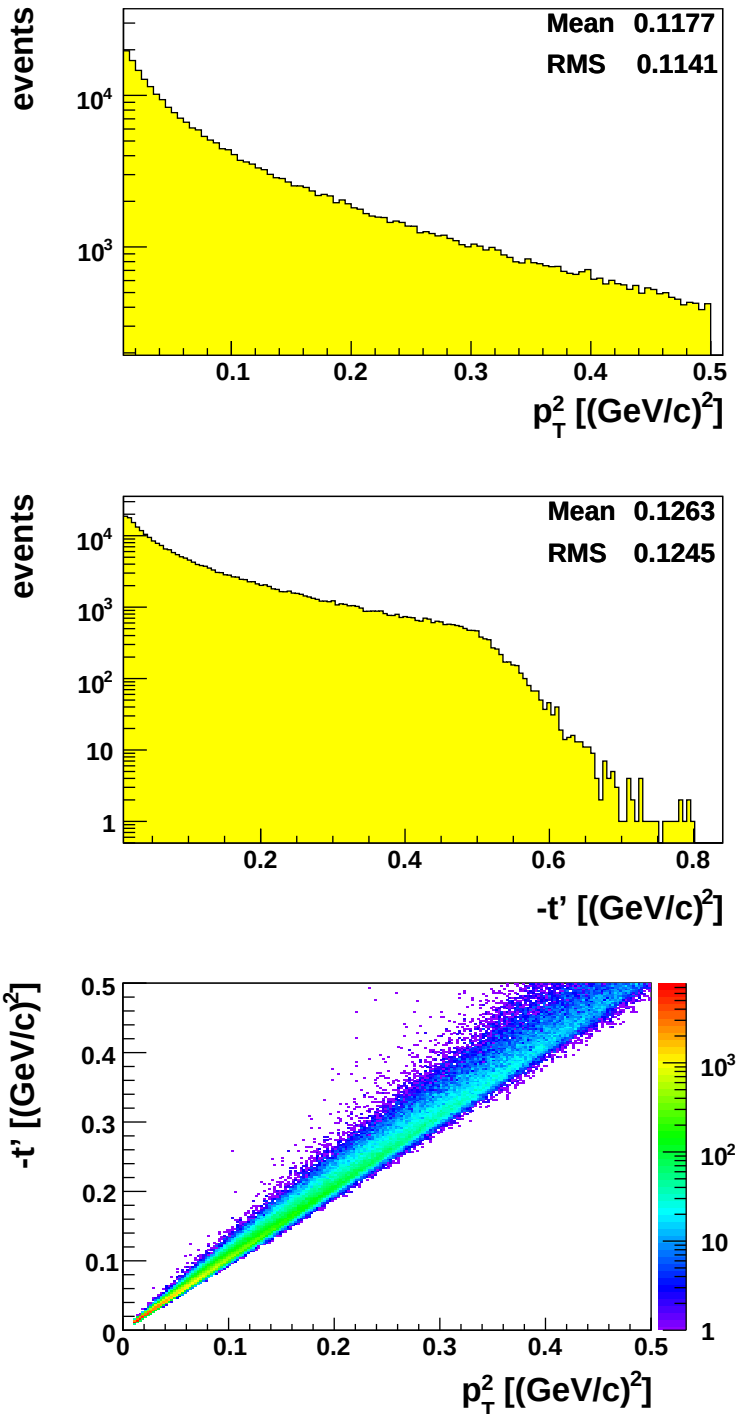

Figure 4.7: Distributions of the kinematic variables p_T^2 and $-t'$ for the final data sample. In addition, to investigate a possible correlation between $-t'$ and p_T^2, the two-dimensional graph is shown. Therein a pronounced correlation for very small values can be seen, which becomes slightly weaker for higher values.

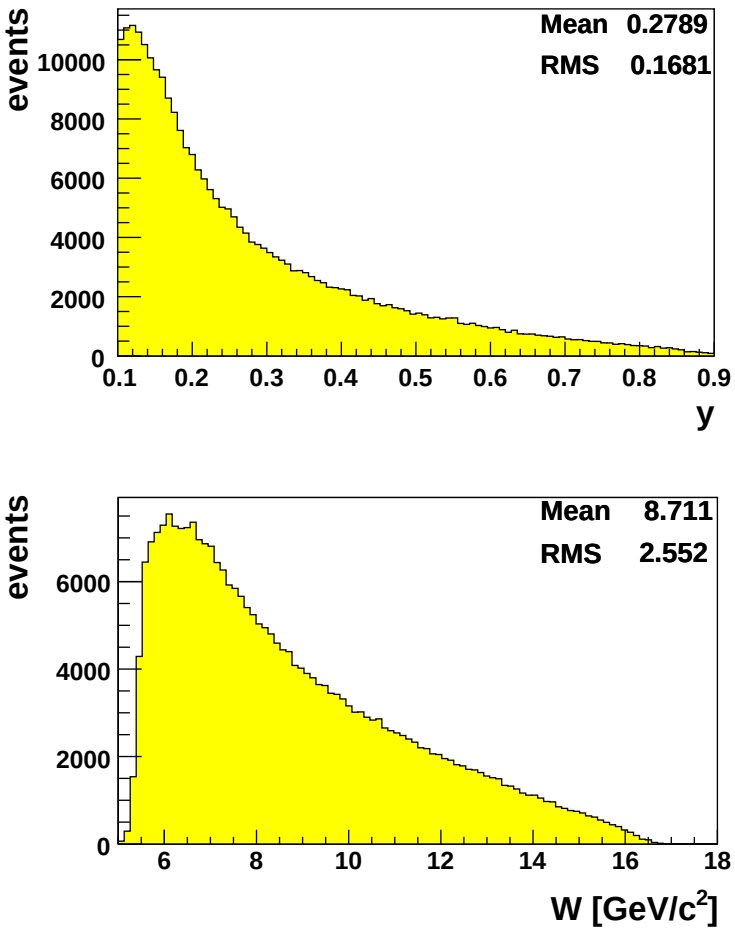

Figure 4.8: Distributions of the kinematic variables y and W for the final data sample. The distribution of the energy fraction y shows that the lepton-nucleon interaction is mediated mainly by virtual photons with small energies (cf. Eq. 4.4).

5 Method for Asymmetry Extraction

This chapter is dedicated to the description of the method used for extracting the amplitude $A_{\mathrm{UT}}^{\sin(\phi_h-\phi_S)}$ of the transverse-target single-spin asymmetry $A_{\mathrm{UT}}(\phi_h-\phi_S)$. Furthermore, diluting factors are described. These quantities have to be taken into account, for correct handling of the experimentally-determined asymmetry, as described in Section 5.4.

5.1 General Information

The transverse-target single-spin asymmetry for production of a longitudinally polarized meson on a transversely (T) polarized target with an unpolarized (U) beam, is defined as (cf. Eq. 2.24 and 2.25)

$$\begin{aligned} A_{\mathrm{UT}}(\phi_h-\phi_S) &= \frac{d\sigma(\phi_h-\phi_S)-d\sigma(\phi_h-\phi_S+\pi)}{d\sigma(\phi_h-\phi_S)+d\sigma(\phi_h-\phi_S+\pi)} \\ &= A_{\mathrm{UT}}^{\sin(\phi_h-\phi_S)}\cdot\sin(\phi_h-\phi_S) \quad , \end{aligned} \tag{5.1}$$

where $A_{\mathrm{UT}}^{\sin(\phi_h-\phi_S)}$ is the amplitude of the asymmetry $A_{\mathrm{UT}}(\phi_h-\phi_S)$ and the azimuthal angles ϕ_h and ϕ_S are defined in the γN-system as described in Section 2.4.1. The asymmetry (5.1) can be related to the event yields per target cell and azimuthal angle $\eta = \phi_h-\phi_S$. For a given target cell u/d (upstream, downstream cell) with polarization ($\pm$) perpendicular upwards/downwards with respect to the beam momentum, the number of events can be written as

$$N_{u/d}^{\pm}(\eta) = c_{u/d}^{\pm}\cdot a_{u/d}^{\pm}(\eta)\cdot\left(1\pm A_{\mathrm{UT,\,raw}}^{\sin(\eta)}\sin(\eta)\right) \quad , \tag{5.2}$$

where $c_{u/d}^{\pm}$ is the product of the total incident muon flux, the number of target particles and the spin-averaged cross-section. The quantities $a_{u/d}^{\pm}(\eta)$ represent the product of angular acceptance and efficiency of the apparatus. The interesting quantity in equation (5.2) is the so-called raw-asymmetry $A_{\mathrm{UT,\,raw}}^{\sin(\phi_h-\phi_S)}$. By taking into account diluting factors (cf. Section 5.4), the extracted raw-asymmetry can

be related to the physical amplitude $A_{\mathrm{UT}}^{\sin(\phi_h-\phi_S)}$ of the transverse-target single-spin asymmetry.

5.2 Double Ratio Method

For the extraction of $A_{\mathrm{UT,raw}}^{\sin(\phi_h-\phi_S)}$ an estimator requiring only weak assumptions on the angular acceptance and efficiency of the apparatus is needed. Therein the time dependence of these quantities can be minimized by using simultaneously taken data from the two oppositely polarized target cells. In addition, the different angular acceptances and efficiencies arising from the two target cells can be minimized by using events from the two target cells with both polarizations, originating from two data-recording periods with reversed target spin configuration.

The estimator fulfilling both requirements, and therefore used for extraction, is the Double Ratio [63]

$$F(\eta) = \frac{N_u^+(\eta) \cdot N_d^+(\eta)}{N_u^-(\eta) \cdot N_d^-(\eta)} \ , \tag{5.3}$$

with relative error

$$\frac{s_{F(\eta)}}{F(\eta)} = \sqrt{\frac{1}{N_u^+(\eta)} + \frac{1}{N_d^+(\eta)} + \frac{1}{N_u^-(\eta)} + \frac{1}{N_d^-(\eta)}} \ . \tag{5.4}$$

$F(\eta)$ is calculated for 16 equidistant bins i in the azimuthal angle η, by using the number of events per angular bin in the upstream/downstream cell (u, d) in dependence on the cell polarization $\pm$.

For the unknown product of angular acceptances and efficiencies, a reasonable assumption (cf. Ref. [63]) is included, relating the ratios of the quantities $a_{u/d}^{\pm}(\eta)$ in the two target cells via:

$$\frac{a_u^-(\eta)}{a_d^+(\eta)} = \frac{a_u^+(\eta)}{a_d^-(\eta)} \Leftrightarrow \frac{a_u^-(\eta)}{a_u^+(\eta)} = \frac{a_d^+(\eta)}{a_d^-(\eta)} \ . \tag{5.5}$$

Therein, the ratio of the product of angular acceptance $a_u^-(\eta)$ in the upstream cell polarized perpendicularly downwards and the corresponding quantity $a_d^+(\eta)$ for the downstream cell polarized perpendicularly upwards, is assumed to be equal to the ratio of these quantities for the two target cells with reversed polarizations.

By using expression (5.2) and the assumption (5.5), the Double Ratio transforms to

$$F(\eta) = C \cdot \frac{(1 + A^{\sin(\eta)}_{\mathrm{UT,\,raw}} \sin(\eta))^2}{(1 - A^{\sin(\eta)}_{\mathrm{UT,\,raw}} \sin(\eta))^2} \quad , \tag{5.6}$$

where C represents the ratio of the quantities $c^{\pm}_{u/d}$ in equation (5.2). The expected value is $C = 1$, because of the assumption on equal beam particle fluxes in both target cells and the relations

$$c^-_u = c^+_d \;\text{ and }\; c^+_u = c^-_d \quad , \tag{5.7}$$

as described in [63].

Finally, after applying a first-order Taylor series approximation in $\sin(\eta)$ around $(\sin(\eta)_0 = 0)$, the expression for the raw-asymmetry $A^{\sin(\eta)}_{\mathrm{UT,\,raw}}$ and thus the fitting function used, becomes

$$F(\eta) \quad = \quad C \cdot \frac{(1 + A^{\sin(\eta)}_{\mathrm{UT,\,raw}} \sin(\eta))^2}{(1 - A^{\sin(\eta)}_{\mathrm{UT,\,raw}} \sin(\eta))^2} \tag{5.8}$$

$$\overset{Taylor}{=} \quad C \cdot (1 + 4 \cdot A^{\sin(\eta)}_{\mathrm{UT,\,raw}} \sin(\eta)) \quad . \tag{5.9}$$

Kinematic Binning

The extraction of the raw-asymmetry $A^{\sin(\eta)}_{\mathrm{UT,raw}}$ is carried out for several ranges of the kinematic variables x_{Bj}, Q^2, p_{T} etc. and finally plotted against mean values of the variables in the specific bin. The purpose of this binning is to investigate possible kinematic dependencies of the amplitude $A^{\sin(\phi_h - \phi_S)}_{\mathrm{UT}}$. Exact ranges of the kinematic variables can be found in Appendix A. In addition, due to this kinematic binning, the amplitude $A^{\sin(\phi_h - \phi_S)}_{\mathrm{UT}}$ is sensitive to dominant contributions in certain kinematic ranges (cf. Section 6.4).

5.3 Data Grouping

In principle, the whole set of data recorded with the transverse-target spin configurations could be combined for the calculation of the Double Ratio (5.3). However, modifications were made to the apparatus and the trigger settings between periods, impeding this kind of combination. Instead, only periods with almost

identical experimental conditions, i.e. neighbouring periods, are combined. Consequently, the ten periods of data-recording, half with the target cell spin configuration $(+,-)$, and the other half with the reversed configuration, are combined to five double periods as depicted in Figure 5.1. In these double periods, the

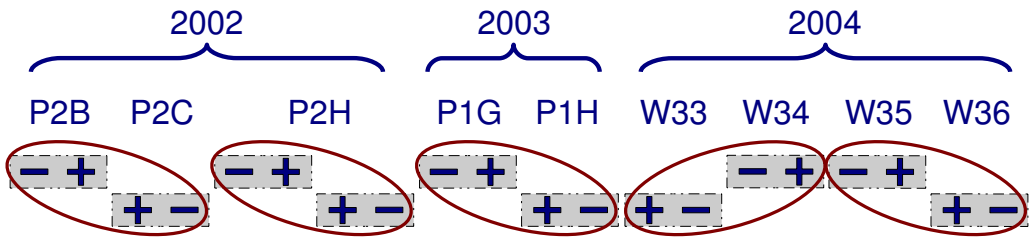

Figure 5.1: Grouping of the data recorded with the transverse-target spin configuration. The total, ten periods are combined to five double-periods, to which the Double Ratio method can be applied.

Double Ratio can be calculated and thus the amplitude of the transverse-target single-spin asymmetry $A_{\mathrm{UT}}^{\sin(phi_h-\phi_S)}$ extracted. A detailed list of these periods can be found in Table 5.1.

Table 5.1: The table shows the periods of data-recording with the corresponding run number. The middle column gives the target spin configurations for the upstream and downstream target cell.

Year	Period	Target Spin Configuration		Run number
		upstream	downstream	
2002	P2B	−	+	21178-21495
	P2C	+	−	21670-21878
	P2H	−	+	23490-23575
	P2H	+	−	23664-23839
2003	P1G	−	+	30772-31038
	P1H	+	−	31192-31524
2004	W33	+	−	38991-39168
	W34	−	+	39283-39545
	W35	−	+	39548-39780
	W36	+	−	39850-39987

5.4 Extracted vs Physical Asymmetry

The dilution factor f and the mean target polarization $\langle P_{\mathrm{T}} \rangle$ are the two major factors diluting the asymmetry $A_{\mathrm{UT}}(\phi_h - \phi_S)$. Therefore, these quantities have to be taken into account for the relation between the experimentally-observed raw-asymmetry $A_{\mathrm{UT,raw}}^{\sin(\phi_h-\phi_S)}$ and the physical amplitude $A_{\mathrm{UT}}^{\sin(\phi_h-\phi_S)}$ of the transverse-target single-spin asymmetry.

5.4.1 Target Polarization $\langle P_{\mathbf{T}} \rangle$

In the case of longitudinal target polarization, the polarizations of the target cells are recurrently measured by five NMR coils along each cell. This recurrent measurement with the available NMR coils is not possible in the transverse mode. Instead, the polarization values are obtained from interpolations of the target polarization curve over the whole beam time. Therefore, the measured target polarizations in the longitudinal mode before and after changing over to the transverse mode are used. The entire list of these polarization values can be found in Appendix A.1. For a short overview, weighted mean target cell polarization values can be found in Table 5.2. These values originate from the final data sample (cf. Chapter 4.6), subdivided into the possible polarizations ($\pm$) of the upstream and downstream target cell.

Table 5.2: Listed below is a short summary of event-weighted mean target polarization values for the final data sample. The four values correspond to the polarization values of a given target cell (u or d) with polarization ($+$ or $-$).

	upstream	downstream
$+$	50.4 %	48.6 %
$-$	46.9 %	43.4 %

5.4.2 Dilution Factor f

The dilution factor f denotes the fraction of interactions in polarizable material. In a naive picture, the target cells are completely filled with ^{6}LiD and the Li nucleus is interpreted as a system consisting of an alpha particle and a polarized deuterium nucleus. These assumptions yield to an expectation of 0.5 for the value of the dilution factor for ^{6}LiD. However, in addition to ^{6}LiD, there are other materials in the volumes of the target cells, mainly ^{3}He and ^{4}He, which serve for the cooling of the target material. In addition, C, F, Ni and Cu nuclei, introduced by

the NMR coils for the polarization measurement, are present in the target region. All these materials need to be taken into account when computing the dilution factor.

Apart from simple contamination, the corresponding cross sections for scattering processes in these materials also need to be taken into account for determining the dilution factor f, which therefore depends on the event kinematics. The dilution factor can be parameterized as a function of x_{Bj} and ν [64, 65]. By using this parameterization, the averaged value was calculated to be $f = 0.38$ in the final data sample. This value is used for relating the extracted quantity $A_{\mathrm{UT,\,raw}}^{\sin(\phi_h-\phi_S)}$ with the physical amplitude $A_{\mathrm{UT}}^{\sin(\phi_h-\phi_S)}$.

5.4.3 Calculation of the physical amplitude $A_{\mathbf{UT}}^{\sin(\phi_h-\phi_S)}$

Using the values for the target polarization $\langle P_{\mathrm{T}} \rangle$ and the dilution factor $f = 0.38$, the extracted raw-asymmetry $A_{\mathrm{UT,raw}}^{\sin(\phi_h-\phi_S)}$ and the physical amplitude $A_{\mathrm{UT}}^{\sin(\phi_h-\phi_S)}$ are related by:

$$A_{\mathrm{UT}}^{\sin(\phi_h-\phi_S)} = \frac{A_{\mathrm{UT,\,raw}}^{\sin(\phi_h-\phi_S)}}{f \cdot \langle P_{\mathrm{T}} \rangle} \quad . \tag{5.10}$$

Due to the kinematic binning, the calculation of this relation is performed for the values of the amplitude $A_{\mathrm{UT}}^{\sin(\phi_h-\phi_S)}$ in the each kinematic bin.

The final value for the amplitude $A_{\mathrm{UT}}^{\sin(\phi_h-\phi_S)}$ for the full statistics and its corresponding error $\sigma_{A_{\mathrm{UT}}}$ are obtained by calculating the weighted mean of results A_i $(i = 1, \ldots, 5)$ from the five double periods via

$$A_{\mathrm{UT}}^{\sin(\phi_h-\phi_S)} = \frac{\sum_i (A_i/\sigma_i^2)}{\sum_i (1/\sigma_i^2)} \quad \text{with} \quad \sigma_{A_{\mathrm{UT}}} = \frac{1}{\sqrt{\sum_i (1/\sigma_i^2)}} \quad , \tag{5.11}$$

where σ_i denote the error on A_i.

6 Results and Discussion

Following the descriptions of event selection and extraction algorithm, this chapter is dedicated to the results for the amplitude $A_{\mathrm{UT}}^{\sin(\phi_h-\phi_S)}$ of the transverse-target single-spin asymmetry $A_{\mathrm{UT}}(\phi_h-\phi_S)$. A review about these results can additionally be found in Ref. [66]. First steps towards the interpretation of these results is presented in Section 6.2 and systematic effects are discussed briefly in Section 6.3. Finally, possible further investigations on different contributions to the amplitude $A_{\mathrm{UT}}^{\sin(\phi_h-\phi_S)}$ are outlined in Section 6.4, accompanied by rough quantitative estimations of these contributions to the final data sample.

6.1 Results

The final result for the amplitude $A_{\mathrm{UT}}^{\sin(\phi_h-\phi_S)}$ of the transverse-target single-spin asymmetry is obtained by the combination of results from the five double periods (cf. Section 5.3). Therefore, the weighted mean values for each kinematic range in x_{Bj}, Q^2, p_{T}, t', E_{miss} and $M_{\pi\pi}$ are calculated (cf. Eq. 5.11) and plotted against the mean kinematic variables in the specific ranges. The results from this procedure are depicted in Figures (6.1–6.3) and the corresponding list of numerical values can be found in Appendix B.

By calculating the overall weighted mean for the individual values in each kinematic bin over the full kinematic range, the value for the amplitude of the transverse-target single-spin asymmetry is

$$A_{\mathrm{UT}}^{\sin(\phi_h-\phi_S)} = 0.016 \pm 0.016(\mathrm{stat.}) \quad . \tag{6.1}$$

Within the statistical error, the value for the amplitude $A_{\mathrm{UT}}^{\sin(\phi_h-\phi_S)}$ is thus compatible with zero. However, this does not necessarily imply the disappearance of the generalized parton distribution E nor of the total angular momentum $J^{u,d}$ of quarks in the nucleon. It rather emphasizes the necessity of kinematic binning, because theoretical predictions for the generalized parton distribution E and the total angular momenta $J^{u,d}$ are limited to certain kinematic ranges (cf. Section 6.2).

Moreover, investigation on the amplitude $A_{\mathrm{UT}}^{\sin(\phi_h-\phi_S)}$ in several kinematic ranges permit interpretation of the results for different contributions to the final data sample (cf. Section 6.4), which otherwise would require reanalyzing of the data with modified kinematic restrictions. In this context, the amplitude $A_{\mathrm{UT}}^{\sin(\phi_h-\phi_S)}$ is also investigated in several kinematic ranges of the energy fraction y. Results of this additional determination can be found in Appendix B.1.

Of particular interest in the context of kinematic binning are the values for the amplitude $A_{\mathrm{UT}}^{\sin(\phi_h-\phi_S)}$ in the last bin of the photon virtuality Q^2 and in the last bin of the Bjorken variable x_{Bj}.

The value of the amplitude in the last bin of x_{Bj}

$$A_{\mathrm{UT}}^{\sin(\phi_h-\phi_S)} = 0.03 \pm 0.04(\mathrm{stat.}) \tag{6.2}$$

is of importance in the context of theoretical predictions, because the kinematically covered range in available theoretical models are limited to a lower value of $x_{Bj} = 0.05$ (cf. Section 6.2). Therefore the last bin of x_{Bj} with a mean value $\langle x_{Bj} \rangle = 0.068$ can be used for the comparison with these theoretical model.

The reason for the interest in the value of the amplitude $A_{\mathrm{UT}}^{\sin(\phi_h-\phi_S)}$ in the last bin of Q^2, with $\langle Q^2 \rangle = 3.92$ (GeV/c)^2,

$$A_{\mathrm{UT}}^{\sin(\phi_h-\phi_S)} = -0.001 \pm 0.037(\mathrm{stat.}) \quad , \tag{6.3}$$

originates from its higher sensitivity to hard exclusive production of longitudinally polarized ρ^0 mesons (cf. Section 6.4) compared to other kinematic regions in Q^2.

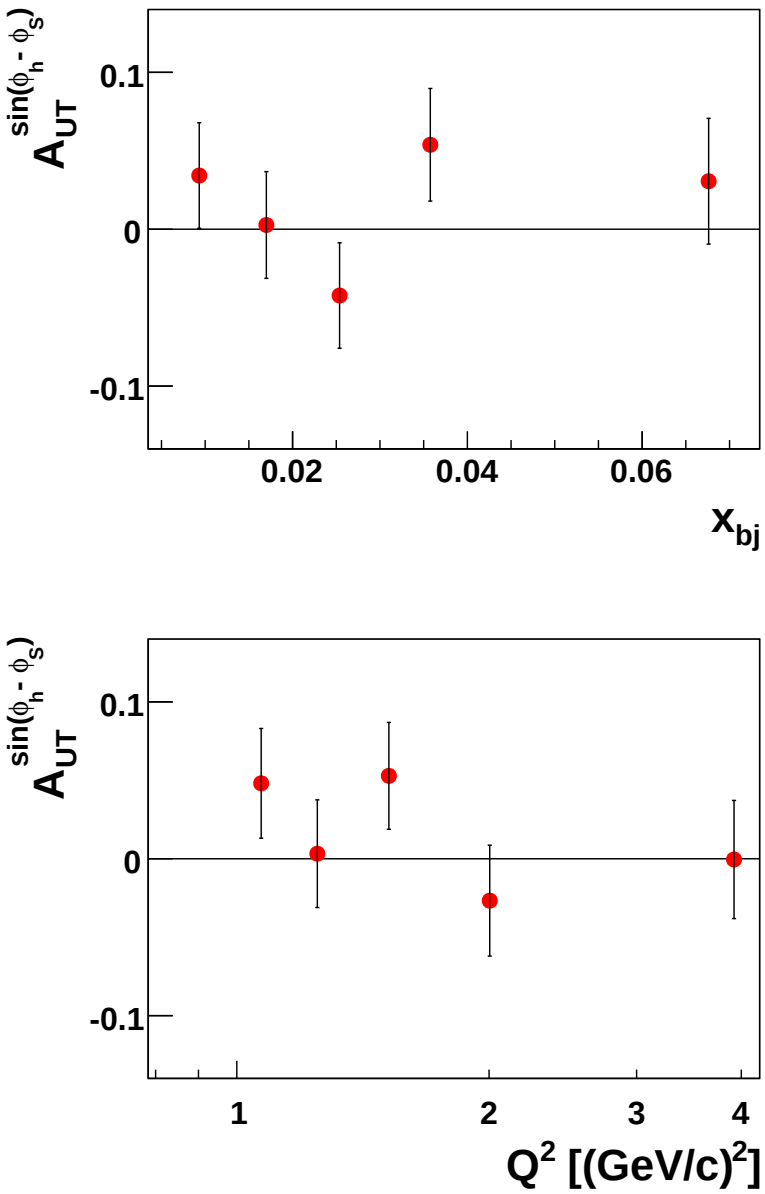

Figure 6.1: Results for the amplitude $A_{\mathrm{UT}}^{\sin(\phi_h-\phi_S)}$ in several kinematic ranges of the variables x_{bj} and Q^2. Of particular interest is the very small value in the last bin of the photon virtuality Q^2 and the value for the last bin in the Bjorken variable x_{bj}.

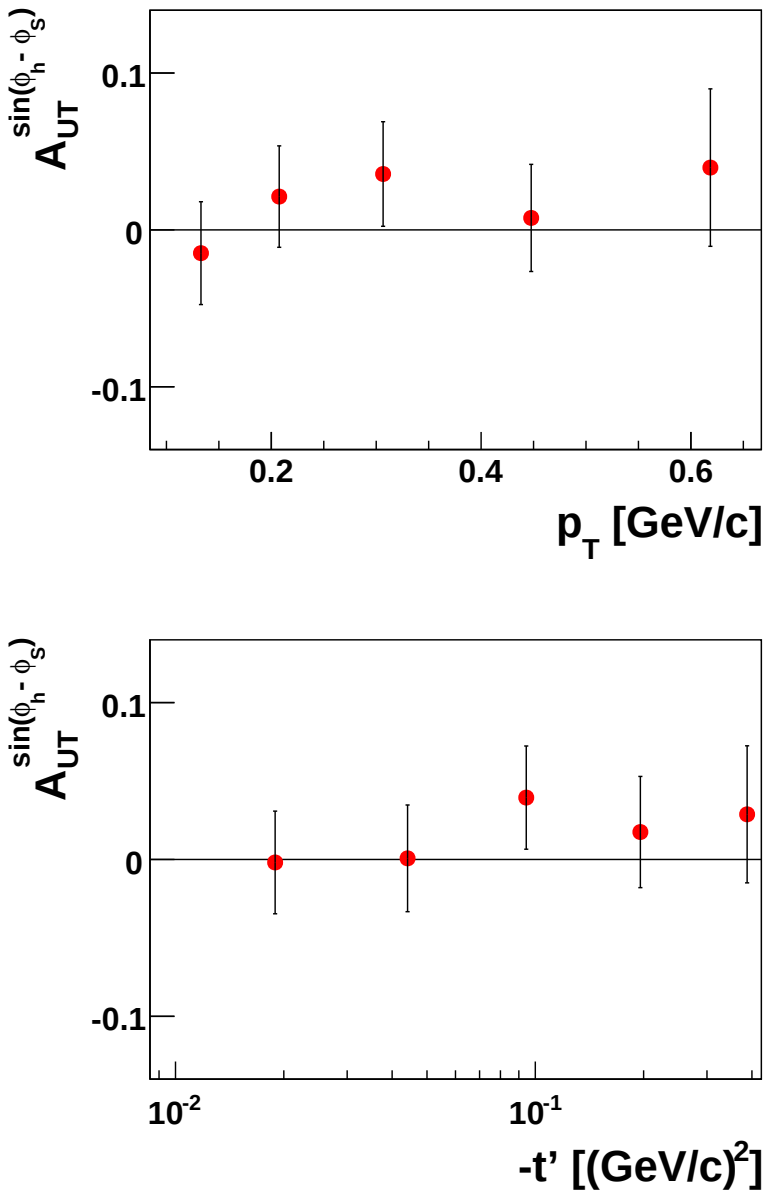

Figure 6.2: Results for the amplitude $A_{\mathrm{UT}}^{\sin(\phi_h-\phi_S)}$ in several kinematic ranges of the kinematic variables p_{T} and $-t'$. The obviously similar behavior of the amplitude values is due to the correlation of the variables $-t'$ and p_{T}^2, depicted in Figure 4.7. The results for higher bins in both variables are without exception positive, which is meaningful for further interpretation, because this kinematic region exhibits a higher sensitivity to incoherently produced ρ^0 mesons (cf. Section 6.4).

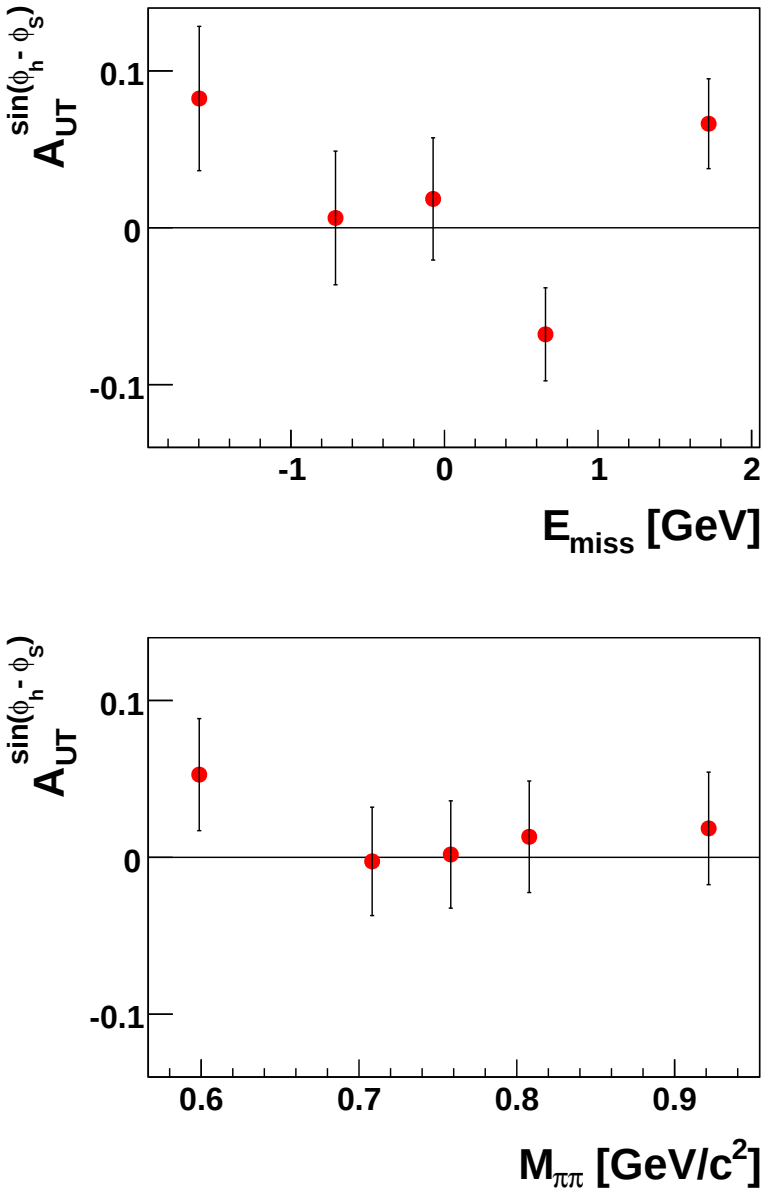

Figure 6.3: Results for the amplitude $A_{\mathrm{UT}}^{\sin(\phi_h-\phi_S)}$ in several kinematic ranges of the variables E_{miss} and $M_{\pi\pi}$. Interesting are the amplitude values in the lower kinematic ranges of the missing energy in the upper plot, because events in this kinematic range exhibit the highest exclusivity.

6.2 Towards a Physical Interpretation

For the interpretation of results, theoretical predictions are needed. These model-calculations for a transversely polarized deuteron target are currently under investigation but were not available at the submission date of this thesis.

However, theoretical predictions for a transversely polarized *proton* target are available [28]. Therein, the generalized parton distributions E^u and E^d are parameterized using the total angular momenta J^u and J^d as free parameters. Following these theoretical predictions, the amplitude of the transverse-target single-spin asymmetry for the production of a longitudinal polarized ρ^0 meson on a transversely polarized proton is mainly sensitive to the combination $(2J^u + J^d)$.

With a fixed value $J^d = 0$, the sensitivity of $A_{\mathrm{UT}}^{\sin(\phi_h - \phi_S)}$ to different values of J^u is presented in Figure 6.4. For all values of J^u, the amplitude exhibits a pronounced sensitivity at $x_{Bj} \simeq 0.35$. Thus, for experimental distinction between the different anticipated values of J^u, a value of $x_{Bj} \simeq 0.35$ seems promising. The mean kinematic values in these predictions are close to the kinematics of COMPASS: $Q^2 \simeq 1.93$ (GeV/c)^2 and $-t' \simeq 0.13$ (GeV/c)^2.

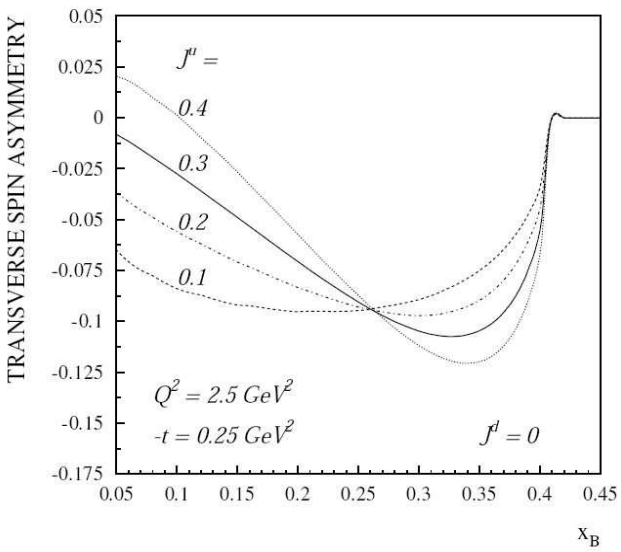

Figure 6.4: Theoretical prediction for the total angular momenta $J^{u,d}$ of quarks in a transversely polarized *proton* target in dependence on the kinematic variable x_{Bj}. With the fixed value $J^d = 0$, the sensitivity of the amplitude $A_{\mathrm{UT}}^{\sin(\phi_h - \phi_S)}$ is shown for several possible values of J^u. For the determination of J^u, experimental results are needed to distinguish between these theoretical predictions. Of importance from the experimental point of view are the mean kinematic variables used for these model-calculations, which are close to COMPASS kinematics ($Q^2 \simeq 1.93$ (GeV/c)^2 and $-t' \simeq 0.13$ (GeV/c)^2).

Recently, COMPASS started measurements on a transversely polarized proton target. As soon as results from this ongoing measurements are ready, they can be interpreted using the upper theoretical predictions. Moreover, as soon as theoretical calculations for the transversely polarized deuteron target are ready, a first determination of the total angular momentum of quarks in the proton and the neutron will be possible.

6.3 Systematic Effects

For quantification of the systematic error, several sources have to be taken into account. In this thesis, these studies are limited to the

- Compatibility of results from the five double periods.
- Validation of the Double Ratio Method, by verifying the assumption on η-independence and on the relations between the quantities $c^{\pm}_{u/d}$ (cf. Section 5.7).

Extended studies of systematic effects can be found in Ref. [67].

Compatibility of results The compatibility of results from the five double periods is checked within the distribution of pulls

$$\frac{A_i - \langle A \rangle}{\sqrt{\sigma^2_{A_i} - \sigma^2_{\langle A \rangle}}} \qquad (i = 1, \ldots, 5) \ , \tag{6.4}$$

where A_i are the results for one of the five kinematic bins in one of the five double periods, $\langle A \rangle$ the weighted mean over the five periods and σ_{A_i} and $\sigma_{\langle A \rangle}$ the corresponding errors. This pull distribution, depicted in Figure 6.5, follows (with RMS = 1.078) an expected Gaussian distribution, which validates the combination of results from the five double period. The 150 entries in this distribution and in Figure 6.6 correspond to values in five bins of six kinematic variables obtained in the five double-periods.

Validation of the Reasonable Assumption The assumption of equal acceptance ratios (cf. Eq. 5.5) and the η-independence and relations of the quantities $c^{\pm}_{u/d}$ in equation (5.7) needs to be validated. Therefore, the distribution of the parameter C appearing in the fitting function (cf. Eq. 5.8) is checked. As depicted in Figure 6.6, the distribution of this parameter is (with RMS = 0.05) centered around $C = 1.04$ and thus close to the expected value $C = 1.0$, which verifies the applicability of the Double Ratio method (cf. Section 5.2).

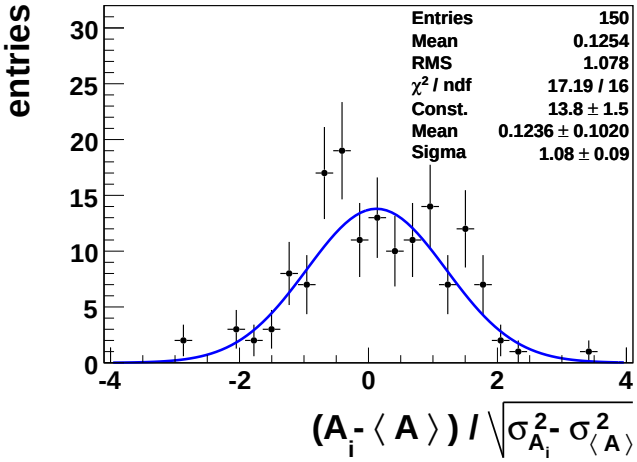

Figure 6.5: Pull distribution for the check of compatibility of the different periods. The fitted Normal distributions (with RMS = 1.078) validate the compatibility of results.

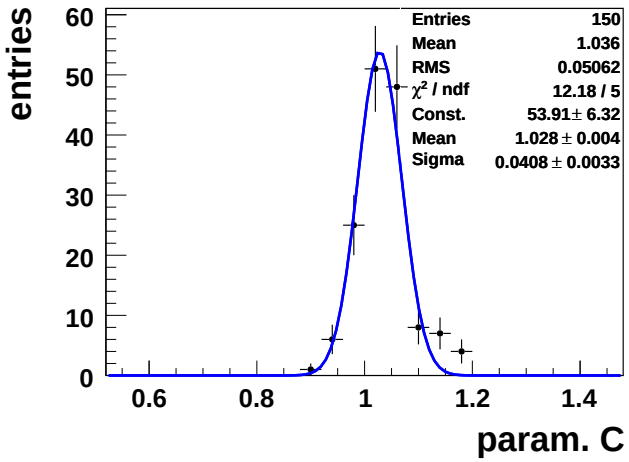

Figure 6.6: Distribution of the parameter C from Eq. (5.8). As expected, the distribution follows (with RMS = 0.05) a Normal distribution centered around $C = 1.04$.

6.4 Further Aspects

The analysis performed leads to first results for the amplitude $A_{\mathrm{UT}}^{\sin(\phi_h - \phi_S)}$ of the transverse-target single-spin asymmetry. In further steps, remaining sources of uncertainties could be minimized by dedicated Monte Carlo studies. Presently, rough estimations of these uncertainties are available, in particular for the dilution of the asymmetry due to non-exclusive background, for contributions of coherently produced ρ^0 mesons and contributions of transversely polarized ρ^0 mesons.

Non-Exclusive Background In addition to exclusively produced ρ^0 mesons, there is a certain amount of non-exclusive background. This cannot be minimized without detection of the recoiling target nucleon, which is not possible as discussed in Section 4.5. However, the contribution of this non-exclusive background in the final data sample can be estimated from the distribution of the missing energy E_{miss}. For this purpose, a function, built as the sum of two Gaussian distributions, was used to fit the distribution of the missing energy in the range of -5.0 GeV to 12.0 GeV. Accordingly, the contribution of non-exclusive background in the range of the final data sample (-2.5 GeV to 2.5 GeV) was estimated to be about 20% (cf. Fig. 6.7).

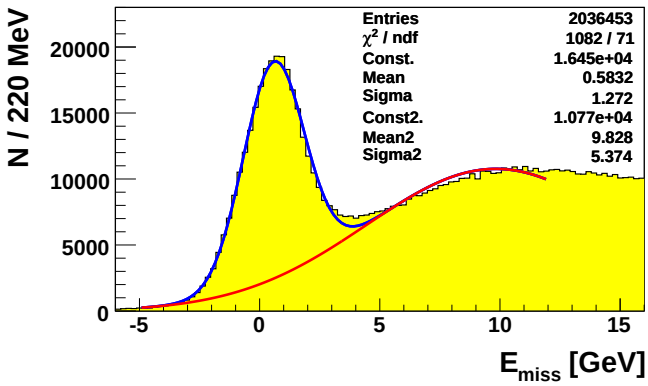

Figure 6.7: Distribution of the missing energy E_{miss} with all restrictions for the final data sample applied except those on this particular variable. This distributions was fitted with a function (blue), built as the sum of two Gaussian distributions, to determine the contributions of non-exclusive background events. The background contributions (red) in the kinematic range of the final data sample (-2.5 GeV to 2.5 GeV) was estimated to about 20%.

The asymmetry of this background was determined by selecting events with $E_{\text{miss}} > 2.5$ GeV and was found to be compatible with zero ($A_{\text{bg}} = 0.007 \pm 0.012$). Considering that this non-exclusive background dilutes the asymmetry, the value for the amplitude $A_{\text{UT}}^{\sin(\phi_h - \phi_S)}$ and its error should be enlarged by a factor of $\sqrt{1 + B/S}$, where B denotes the contribution of background and S the contribution of the signal respectively. To be more precise, this correction needs to be performed in dependence of the specific contributions in each kinematic range (cf. Ref. [60]).

Incoherent Background In addition to non-exclusive background, there are contributions from coherently produced ρ^0 mesons. The term *coherent* describes processes, where a virtual photon interacts with a deuteron, which remains intact

after the interaction. For these kind of reactions the theoretical prediction of the total angular momenta of quarks in one individual nucleon (proton or neutron) are not possible with the underlying theory. The highest contributions of these coherent events are present in processes with small values of $-t'$, i.e. where the momentum transfer to the target is small. In this context, the advantage of kinematic binning becomes evident again, where results for the amplitude $A_{\mathrm{UT}}^{\sin(\phi_h-\phi_S)}$ are presented for different kinematic regions of t' (cf. Fig. 6.1). Therein, the values for the amplitude in higher kinematic ranges are more sensitive to *incoherently* produced ρ^0 mesons [61].

Longitudinally vs transversely polarized photons The factorization of dynamics into hard and soft sub-processes for hard exclusive meson production was only proven for longitudinally polarized photons (cf. Section 2.4). As mentioned before, the polarization of the virtual photon can be determined from the angular distribution of the ρ^0 meson decay products. Therein, spin density matrix elements for the meson decay can be extracted. Using the concept of SCHC (cf. Section 2.4), the ratio of longitudinally and transversely polarized photons $R = \frac{\sigma_{\mathrm{L}}}{\sigma_{\mathrm{T}}}$ can be related to a spin density matrix element extractable from the distribution of the invariant mass of the hadronic final state $W(\cos(\theta))$ [60]. A brief discussion about the definition of the involved term $\cos(\theta)$ can be found in Appendix C.

For the determination of the ratio R, a precise knowledge of the acceptance-function of the apparatus is needed. However, experimental results (cf. Fig. 6.8) support the dominance of longitudinally polarized photons in higher kinematic ranges of Q^2.

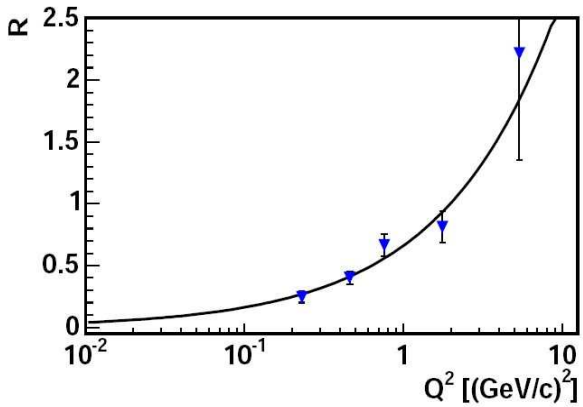

Figure 6.8: Functional Q^2 dependence of the ratio $R = \sigma_L/\sigma_T$ [60]. At the mean kinematic Q^2 range of COMPASS, both contributions are equal, while above $Q^2 \simeq 2$ (GeV/c)^2 the contributions of longitudinally polarized photons dominate.

At the mean kinematic value $Q^2 \simeq 1.93\ (\mathrm{GeV/c})^2$ in the final data sample, both contributions are of the order of 50%. Above $Q^2 \simeq 2\ (\mathrm{GeV/c})^2$ the contribution of events induced by longitudinally polarized photons dominate. In this context, the very small value in the last bin of Q^2 (cf. Eq. 6.3), shows the highest sensitivity to hard exclusive scattering processes involving longitudinally polarized photons.

7 Summary

Unpolarized scattering experiments lead to profound knowledge about the very complex structure of the nucleon, encoded in unpolarized parton distribution functions. Great progress in determining the even more complicated spin structure of the nucleon was made in polarized deep inelastic scattering experiments. Results for the polarized parton distribution functions, encoding the *spin* structure of the nucleon, lead to an accurate value of the quark helicity contribution $\Delta\Sigma$, and a precise determination of the gluon helicity contribution ΔG is currently under experimental investigation.

On the other hand, the contributions of orbital angular momenta to the nucleon spin have still not been determined. About a decade ago, a possible chance to pin down these contributions was proposed. With a similar technique to that employed in deep inelastic scattering processes, the nucleon structure, probed in exclusive processes, can be parameterized in terms of generalized parton distribution functions. As the term *generalized* implies, these functions reduce in a certain limit, the forward limit, to the usual parton distribution functions. In addition, these hitherto unknown generalized counterparts of the well-determined parton distribution functions conceal a huge potential to study new aspects of the nucleon structure.

Of special interest in this context is a sum rule for generalized parton distributions, deduced by Ji, which may provide access to the total angular momenta of quarks in the nucleon and thus, with additional knowledge of the helicity contributions, to the missing contribution of the orbital angular momentum L_q of quarks to the spin of the nucleon.

One key observable to access the total angular momenta is the transverse-target single-spin asymmetry, which appears in reactions like hard exclusive production of ρ^0 meson. The high interest in this observable originates from its unique linear dependence on the generalized parton distribution E, which plays a very prominent role in Ji's sum rule and can hardly be determined from other observables.

The extraction of the amplitude $A_{\mathrm{UT}}^{\sin(\phi_h-\phi_S)}$ of the transverse-target single-spin asymmetry for hard exclusive ρ^0 meson production on a transversely polarized deuteron target was the purpose of this thesis. To extract the amplitude, a ded-

icated event selection was devised and an extraction algorithm, based on the Double Ratio method, was built. All these efforts lead to the very first result for the amplitude of the transverse-target single-spin asymmetry, which is within the statistical error compatible with zero:

$$A_{\mathrm{UT}}^{\sin(\phi_h-\phi_S)} = 0.016 \pm 0.016(\mathrm{stat.}) \quad . \tag{7.1}$$

A comparison of this very first result with theoretical predictions will be one of the very first steps to determine the total angular momenta of quarks in the nucleon.

To investigate possible kinematic dependencies, the amplitude was extracted in several ranges of the kinematic variables. The results for $A_{\mathrm{UT}}^{\sin(\phi_h-\phi_S)}$ in the specific ranges are sensitive to different contributions in the final data sample. For example, scattering processes characterized by larger values for the photon virtuality Q^2 exhibit the highest sensitivity to hard exclusive ρ^0 meson production induced by a longitudinally polarized virtual photon. Beside the contribution of events induced by transversely polarized photons, a certain amount of non-exclusive background is contained in the final data sample. Its contribution can be estimated to roughly 20%. The very small extracted value of the amplitude for the non-exclusive background indicates, that the physical amplitude $A_{\mathrm{UT}}^{\sin(\phi_h-\phi_S)}$ is diluted due to the contribution of non-exclusive background events.

Further investigations on the amplitude $A_{\mathrm{UT}}^{\sin(\phi_h-\phi_S)}$ might improve the distinction between the different contributions in the final data sample. In particular, the determination of the contributions of transversely polarized ρ^0 mesons, non-exclusive background and coherently produced ρ^0 mesons could be subject of future considerations. An improvement in the statistical error, however, would require further measurements with a transversely polarized deuteron target, which are presently not planned.

COMPASS recently started investigation on the nucleon spin structure with a transversely polarized proton target. As soon as corresponding results for the amplitude $A_{\mathrm{UT}}^{\sin(\phi_h-\phi_S)}$ are ready, the total angular momenta of quarks in the proton and the neutron will become accessible. In further steps, an upgrade of the COMPASS apparatus will allow the measurement of deeply virtual Compton scattering, a second promising process for accessing generalized parton distribution functions. With those results, the COMPASS collaboration will contribute to an ever deeper understanding of contributions to the spin of the nucleon.

List of Figures

List of Tables

A Table Of Kinematic Ranges and Target Polarization Values

A.1 Kinematic Ranges

In the following the kinematic ranges for the extraction of the amplitude $A_{\mathrm{UT}}^{\sin(\phi_h-\phi_S)}$ are presented. In particular, the ranges of the variables x_{Bj}, Q^2, p_{T}, E_{miss}, $M_{\pi\pi}$ and t' are listed below.

$0.0000 <$	x_{Bj}	< 0.0132	$0.100 <$	p_{T}	< 0.166
$0.0132 \leq$	x_{Bj}	< 0.0210	$0.166 \leq$	p_{T}	< 0.253
$0.0210 \leq$	x_{Bj}	< 0.0300	$0.253 \leq$	p_{T}	< 0.368
$0.0300 \leq$	x_{Bj}	< 0.0434	$0.368 \leq$	p_{T}	< 0.548
$0.0434 \leq$	x_{Bj}		$0.548 \leq$	p_{T}	

$1.000 <$	Q^2	< 1.145	$0.000 <$	$-t'$	< 0.029
$1.145 \leq$	Q^2	< 1.363	$0.029 \leq$	$-t'$	< 0.063
$1.363 \leq$	Q^2	< 1.704	$0.063 \leq$	$-t'$	< 0.135
$1.704 \leq$	Q^2	< 2.424	$0.135 \leq$	$-t'$	< 0.279
$2.424 \leq$	Q^2		$0.279 \leq$	$-t'$	

$-2.500 <$	E_{miss}	< -1.072	$0.400 <$	$M_{\pi\pi}$	< 0.673
$-1.072 \leq$	E_{miss}	< -0.410	$0.673 \leq$	$M_{\pi\pi}$	< 0.736
$-0.410 \leq$	E_{miss}	< 0.226	$0.736 \leq$	$M_{\pi\pi}$	< 0.780
$0.226 \leq$	E_{miss}	< 1.104	$0.780 \leq$	$M_{\pi\pi}$	< 0.843
$1.104 \leq$	E_{miss}	< 2.500	$0.843 \leq$	$M_{\pi\pi}$	< 1.100

A.2 Target Polarization Values

A full list of measured target cell polarization values can be found below. The values used for the correction (cf. Eq. 5.10) of the extracted raw-asymmetry are calculated as an event-weighted mean of these values.

Table A.1: Polarization values of upstream and downstream target cells for the data-recording periods with a transverse target spin configuration. The values of the target cell polarizations therein are percent values.

Periods	Runs	Polarization [%]	
		upstream	downstream
P2B	21178-21207	−49.79	54.58
P2B	21333-21393	−47.79	47.40
P2B	21407-21495	−47.09	46.33
P2C	21670-21765	52.50	−44.09
P2C	21777-21878	50.36	−43.06
P2H	23490-23575	−49.83	52.11
P2H	23664-23839	47.45	−41.41
P1G	30772-31038	−49.70	52.78
P1H	31192-31247	49.39	−42.60
P1H	31277-31524	51.31	−44.63
W33	38991-39168	50.70	−43.52
W34	39283-39290	−44.80	45.97
W34	39325-39430	−38.60	40.35
W34	39480-39545	−46.14	47.41
W35	39548-39780	−46.44	47.44
W36	39850-39987	49.89	−42.76

B Numerical values for the extracted amplitude $A_{\mathrm{UT}}^{\sin(\phi_h-\phi_S)}$

The values obtained in this analysis for the amplitude $A_{\mathrm{UT}}^{\sin(\phi_h-\phi_S)}$ of the transverse-target single-spin asymmetry in hard exclusive production of a ρ^0 meson are depicted in Fig. (6.1–6.3). The corresponding numerical values are listed below.

Table B.1: Results for the amplitude $A_{\mathrm{UT}}^{\sin(\phi_h-\phi_S)}$ of the transverse-target single-spin asymmetry in ranges of the kinematic variables x_{Bj}, Q^2, p_{T}, $-t'$, E_{miss} and $M_{\pi\pi}$. In the second and fifth column, the mean values for the kinematic variable in the specific bins are listed. The third and the fourth (respectively sixth and seventh) column contains the values for the amplitude $A_{\mathrm{UT}}^{\sin(\phi_h-\phi_S)}$ and the corresponding statistical errors.

#Bin	$\langle x_{Bj}\rangle$	value	stat. error	$\langle Q^2\rangle$	value	stat. error
1	0.0093	0.0342	0.0337	1.0693	0.0481	0.0350
2	0.0170	0.0027	0.0340	1.2477	0.0032	0.0343
3	0.0254	-0.0423	0.0336	1.5187	0.0529	0.034
4	0.0358	0.0538	0.0359	2.0038	-0.0267	0.0353
5	0.0676	0.0306	0.0401	3.9210	-0.0005	0.0377
#Bin	$\langle p_{\mathrm{T}}\rangle$	value	stat. error	$\langle E_{\mathrm{miss}}\rangle$	value	stat. error
1	0.1330	-0.0148	0.0328	-1.5971	0.0824	0.0460
2	0.2075	0.0212	0.0323	-0.7096	0.0063	0.0426
3	0.3066	0.0356	0.0333	-0.0740	0.0184	0.0390
4	0.4478	0.0076	0.0341	0.6579	-0.0680	0.0297
5	0.6186	0.0397	0.0502	1.7203	0.0663	0.0286
#Bin	$\langle M_{\pi\pi}\rangle$	value	stat. error	$\langle -t'\rangle$	value	stat. error
1	0.5988	0.0527	0.0357	0.0189	-0.0019	0.0327
2	0.7083	-0.0026	0.0346	0.0442	0.0007	0.0340
3	0.7582	0.0018	0.0342	0.0943	0.0394	0.0329
4	0.8079	0.0131	0.0355	0.1959	0.0175	0.0354
5	0.9218	0.0185	0.0359	0.3879	0.0288	0.0437

B.1 Result for $A_{\mathrm{UT}}^{\sin(\phi_h-\phi_S)}$ in ranges of the energy fraction y

The extraction of the amplitude $A_{\mathrm{UT}}^{\sin(\phi_h-\phi_S)}$ of the transverse-target single-spin asymmetry was additionally performed in ranges of the kinematic variable y. Results for the full 2002-2004 statistics are depicted in Figure B.1 and the corresponding numerical values are listed below.

#Bin	$\langle y \rangle$	value	stat. error
1	0.1455	0.0169	0.0246
2	0.2446	0.0081	0.0325
3	0.3461	0.0072	0.0430
4	0.4465	0.0172	0.0513
5	0.6329	0.0503	0.0435

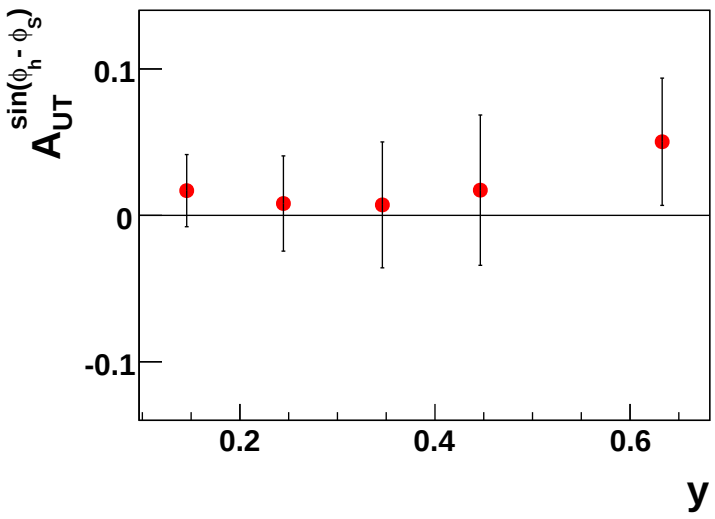

Figure B.1: Result for the amplitude of the transverse-target single-spin asymmetry $A_{\mathrm{UT}}^{\sin(\phi_h-\phi_S)}$ in ranges of the kinematic variable y.

C Calculation of $\cos(\theta)$

For separating contributions of longitudinally and transversely polarized photons, Monte Carlo simulations for the detector acceptance-function are needed. As discussed in Section 6.4, the angular distribution of the ρ^0 meson decay can be used for the separation of the two contributions. Therefore, the distribution of the invariant mass of the final hadronic state $W(\cos(\theta))$ in dependence on $\cos(\theta)$ is investigated. This appendix is dedicated to the derivation of a new method for the calculation of $\cos(\theta)$.

Originally, the angle 'θ' was defined is by Schilling and Wolf [68] in the ρ^0 rest-frame, as the angle between the direction of the positively charged decay pion π^+ and the negative direction of the momentum vector of the recoiling target particle. Accordingly, the four-momenta of the π^+ meson and of the final state nucleon have to be boosted into the ρ^0 rest-frame. Therefore, the four-momentum of the final state nucleon has to be reconstructed using four-momentum conservation $P' = P + q - \rho$, where in addition to the four-momenta P of the initial state nucleon and q of the virtual photon the four-momentum ρ of the ρ^0 meson is needed. The latter is not directly observable, but is also reconstructed using the four-momenta of its decay particles.

In a more direct determination, $\cos(\theta)$ is calculated by using the momentum vector of the ρ^0 in the γN-system (GNS). In this system, the momentum vectors of the initial state nucleon and of the photon are co-linear, implying a co-linearity of the momentum-vectors of the final state nucleon and of the ρ^0 meson.

Before using this method, a proof for equality of the negative direction of the final state nucleon momentum vector in the ρ^0 rest-frame and the direction of the momentum vector of the ρ^0 meson in GNS is needed.

Proof. For simplicity the momentum vector of the ρ^0 meson in GNS is assumed to be aligned in $\hat{z}$ direction.

$$\rho_{GNS} = (E_\rho, 0, 0, \rho_z) = \gamma_0 c M_\rho \cdot (1, 0, 0, \beta_0) \tag{C.1}$$

and consequently

$$\begin{aligned} P'_{GNS} &= (E_{P'}, 0, 0, P_z) = (E_{P'}, 0, 0, -\rho_z) \\ &= \gamma_0 c \cdot (M_P, 0, 0, -M_\rho \beta_0) \end{aligned} \tag{C.2}$$

where $\beta_0 = |\rho_z|/c$ and $\gamma_0 = (1 - \beta_0^2)^{-1/2}$. The transformation into the ρ^0 rest-frame is given by the matrix

$$\mathbf{L} = \begin{pmatrix} \gamma_0 & 0 & 0 & -\gamma_0\beta_0 \\ 0 & 1 & 0 & 0 \\ 0 & 0 & 1 & 0 \\ -\gamma_0\beta_0 & 0 & 0 & \gamma_0 \end{pmatrix}$$

Applying this matrix to the four-momentum of the ρ^0 meson in the GNS its four-momentum vector in the rest-frame is given by $\rho_{RF} = (M_\rho c, 0, 0, 0)$, where the subscript RF denotes the ρ^0 meson rest-frame.

More interesting is the transformation of the final state nucleon momentum vector

$$P'_{RF} = \mathbf{L}\, P' = \gamma_0^2 c \cdot ((M_P + M_\rho \beta_0^2), 0, 0, -\beta_0(M_P + M_\rho)) \tag{C.3}$$

Comparing the momentum vectors in Equation (C.1) and (C.3)

$$\begin{aligned} \vec{\rho}_{GNS} &= \gamma_0 c M_\rho \cdot (0, 0, \beta) \\ -\vec{P'}_{RF} &= \gamma_0^2 c (M_P + M_\rho) \cdot (0, 0, \beta) \end{aligned}$$

the equality of the corresponding normalized vectors is directly evident. Consequently, the calculation of $\cos(\theta)$ is equivalent for both vectors

$$\cos(\theta) = \frac{\vec{\pi}_{RF} \cdot (-\vec{P'})_{RF}}{|\vec{\pi}_{RF}| \cdot |\vec{P'}_{RF}|} = \frac{\vec{\pi}_{RF} \cdot \vec{\rho}_{GNS}}{|\vec{\pi}_{RF}| \cdot |\vec{\rho}_{GNS}|} \quad .$$

□

D Results for $A_{\mathrm{UT}}^{\sin(\phi_h+\phi_S-\pi)}$

In equivalence to the extraction of the amplitude $A_{\mathrm{UT}}^{\sin(\phi_h-\phi_S)}$ of the transverse-target single-spin asymmetry, another azimuthal amplitude was extracted from the final data sample in the same ranges of the kinematic variables. For the relation between the physical amplitude $A_{\mathrm{UT}}^{\sin(\phi_h+\phi_S-\pi)}$ and the extracted raw-asymmetry $A_{\mathrm{UT},raw}^{\sin(\phi_h+\phi_S-\pi)}$ an additional diluting factor, the depolarization factor $D_{\mathrm{NN}}(y) = (1-y)/(1-y+y^2/2)$ has to be taken into account, which is available on an event-by-event basis. Hence, the azimuthal amplitude is calculated via:

$$A_{\mathrm{UT}}^{\sin(\phi_h+\phi_S-\pi)} = \frac{A_{\mathrm{UT,raw}}^{\sin(\phi_h+\phi_S-\pi)}}{f \cdot \langle P_{\mathrm{T}} \rangle \cdot \langle D_{\mathrm{NN}} \rangle} \quad , \tag{D.1}$$

where $\langle D_{\mathrm{NN}} \rangle$ is calculated as the event weighted mean in the specific kinematic range. Results for this extraction are depicted in Figure D.1 and D.2.

Similar to the amplitude $A_{\mathrm{UT}}^{\sin(\phi_h-\phi_S)}$ the overall weighted mean value for the amplitude is small and within the statistical error compatible with zero:

$$A_{\mathrm{UT}}^{\sin(\phi_h+\phi_S-\pi)} = -0.020 \pm 0.016(\mathrm{stat.}) \tag{D.2}$$

This is in good agreement with theoretical predictions, which anticipate the disappearance of this amplitude.

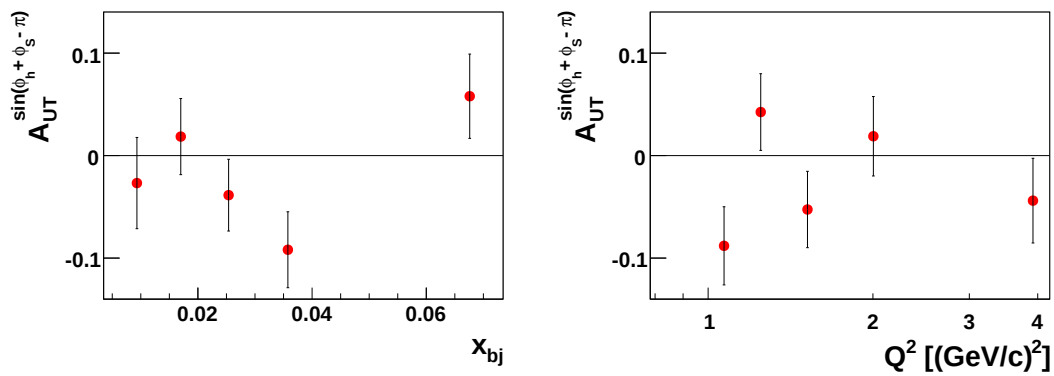

Figure D.1: Results for the amplitude $A_{\mathrm{UT}}^{\sin(\phi_h+\phi_S-\pi)}$ in certain ranges of the kinematic variables x_{Bj} and Q^2.

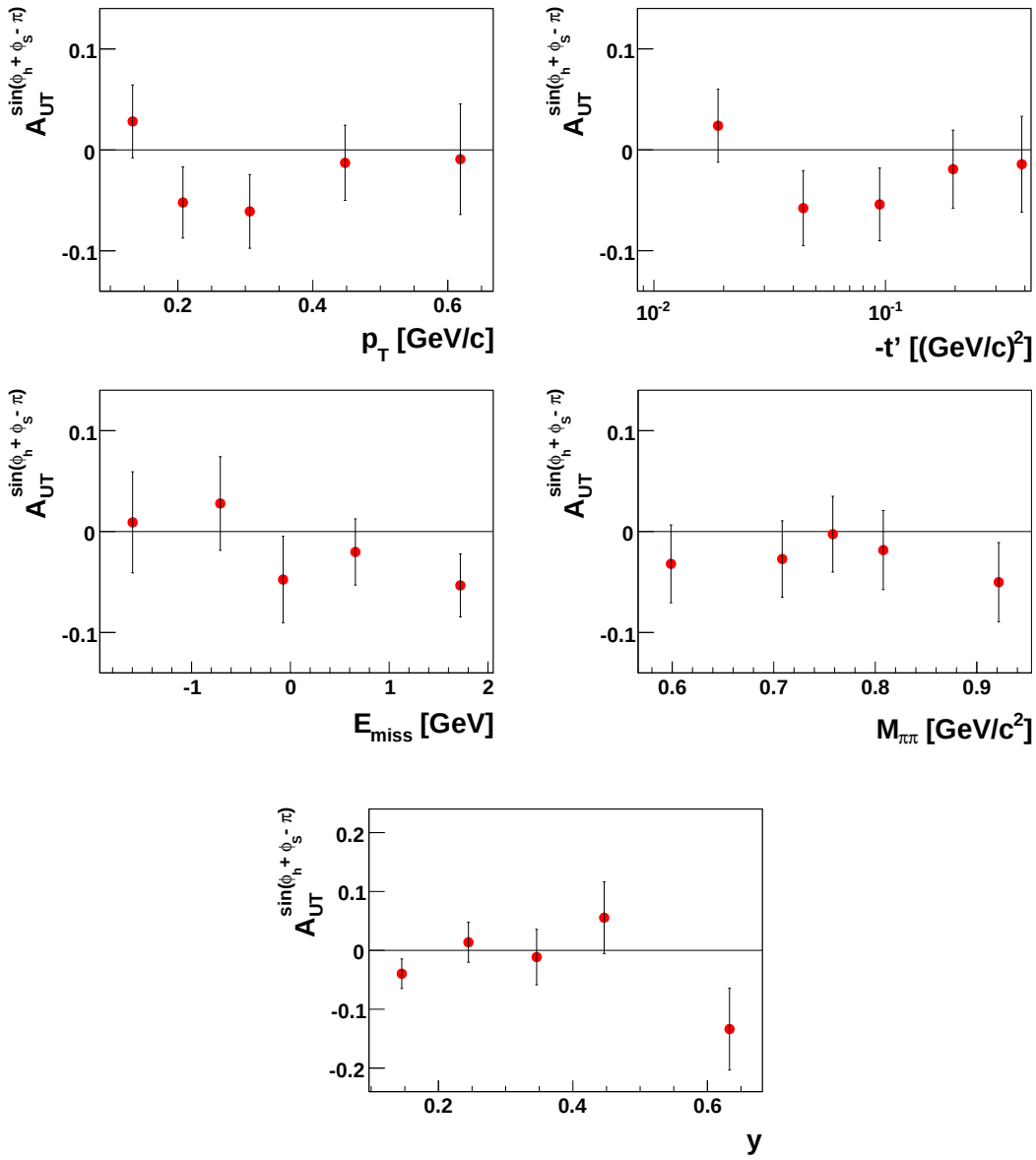

Figure D.2: Results for the amplitude $A_{\mathrm{UT}}^{\sin(\phi_h+\phi_S-\pi)}$ in certain ranges of the kinematic variables p_{T}, t', E_{miss}, $M_{\pi\pi}$ and y. Therein the range in the y-axis for the graph in y is widened.

Bibliography

[1] M. Gell-Mann, *A schematic model of baryons and mesons*, Phys. Lett. 8, (214-215), 1964.

[2] G. Zweig, *An SU(3) Model for strong interaction symmetry and its breaking*, 1964, CERN-TH-401 and CERN-TH-412.

[3] J. Ashman et al., *A measurement of the spin asymmetry and determination of the structure function g(1) in deep inelastic muon proton scattering*, Phys. Lett. B206, (364-370), 1988.

[4] R. L. Jaffe and A. Manohar, *The G(1) Problem: Fact And Fantasy On The Spin Of The Proton*, Nucl. Phys. B337, (509-546), 1990.

[5] V. Yu. Alexakhin et al., *The Deuteron Spin-dependent Structure Function g_1^d an its First Moment*, Phys. Lett. B647, (8-17), 2007. hep-ex/0609038.

[6] E. S. Ageev et al., *Gluon polarization in the nucleon from quasi-real photoproduction of high-p_T hadron pairs*, Phys. Lett. B633, (25-32), 2006. hep-ex/0511028.

[7] D. Müller, D. Robaschik, B. Geyer, F. M. Dittes, and J. Horejsi, *Wave functions, evolution equations and evolution kernels from light-ray operators of QCD*, Fortschr. Phys. 42, (101), 1994. hep-ph/9812448.

[8] A. V. Radyushkin, *Nonforward Parton Distributions*, Phys. Rev. D56, (5524-5557), 1997. hep-ph/9704207.

[9] X. Ji, *Gauge-Invariant Decomposition of Nucleon Spin*, Phys. Rev. Lett. 78, (610-613), 1997. hep-ph/9603249.

[10] R.G. Roberts, *The Structure of the Proton: Deep Inelastic Scattering*, Cambridge Monographs on Mathematical Physics. Cambridge University Press, 1990.

[11] J. C. Collins, D. E. Soper, and G. Sterman, *Factorization of hard processes in QCD*, Adv. Ser. Direct. High Energy Phys. 5, (1-91), 1988. hep-ph/0409313.

[12] R. D. Field, *Applications of Perturbative QCD*, Frontiers In Physics. Addison-Wesley Publishing Company, 1989.

[13] A. Manohar, *An Introduction to Spin Dependent Deep Inelastic Scattering*, 1992, Lectures presented at the Lake Louise Winter Institute, hep-ph/9204208.

[14] R. P. Feynman, *Very high-energy collisions of hadrons*, Phys. Rev. Lett. 23, (1415-1417), 1969.

[15] C. G. Callan and D. J. Gross, *High-Energy Electroproduction and the Constution of the Electric Current*, Phys. Rev. Lett. 22, (156-159), 1969.

[16] J. D. Bjorken and E. A. Paschos, *Inelastic Electron Proton and Gamma Proton Scattering and the Structure of the Nucleon*, Phys. Rev. 185, (1975-982), 1969.

[17] M. Diehl, *Generalized Parton Distributions*, Phys. Rept. 388, (41-277), 2003. hep-ph/0307382.

[18] R. Jakob, *Transverse Momenta in Hard Scattering Processes*, Postdoctoral thesis, University of Wuppertal, November 2002.

[19] X. Ji and J. Osborne, *One-loop corrections and all order factorization in deeply virtual Compton scattering*, Phys. Rev. D58, (094018), 1998. hep-ph/9801260.

[20] J. C. Collins and A. Freud, *Proof of factorization for deeply virtual Compton scattering in QCD*, Phys. Rev. D59, (074009), 1999. hep-ph/9801262.

[21] J. C. Collins, L. Frankfurt, and M. Strikman, *Factorization for hard exclusive electroproduction of mesons in QCD*, Phys. Rev. D56, (2982-3006), 1997. hep-ph/9611433.

[22] M. Diehl, T. Gousset, B. Pire, and O. Teryaev, *Probing partonic structure in $\gamma^*\gamma \to \pi\pi$ near threshold*, Phys. Rev. Lett. 81, (1782-1785), 1998. hep-ph/9805380.

[23] X. Ji, *Off-forward parton distributions*, J. Phys. G24, (1181-1205), 1998. hep-ph/9807358.

[24] A. V. Radyushkin, *Generalized parton distributions*, 2000, hep-ph/0101225.

[25] J. C. Collins, *Light-cone variables, rapidity and all that*, 1997, hep-ph/9705393.

[26] M. Diehl, T. Feldmann, R. Jakob, and P. Kroll, *Linking Parton Distributions to Form Factors and Compton Scattering*, Eur. Phys. J. C8, (409-434), 1999. hep-ph/9811253.

[27] B. W. Filippone and X. Ji, *The Spin Structure Of The Nuleon*, Adv. Nucl. Phys. 26, (1-88), 2001. hep-ph/0101224.

[28] K. Goeke, M. V. Polyakov, and M. Vanderhaeghen, *Hard Exclusive Reactions and the Structure of Hadrons*, Prog. Part. Nucl. Phys. 47, (401-515), 2001. hep-ph/0106012.

[29] S. J. Brodsky, F. E. Close, and J. F. Gunion, *Phenomenology of Photon Processes, Vector Dominance, and Crucial Tests for Parton Models*, Phys. Rev. D6, (177-189), 1972.

[30] F. Bradamante (Ed.), G. Mallot (Ed.), and S. Paul (Ed.), *Workshop on future physics @ COMPASS, CERN, Geneva, Switzerland, 26-27 Sep 2002: Proceedings*, CERN-2004-011.

[31] K. Ackerstaff et al., *Flavor decomposition of the polarized quark distributions in the nucleon from inclusive and semi-inclusive deep inelastic scattering*, Phys. Lett. B464, (123-134), 1999. hep-ex/9906035.

[32] A. Airapetian et al., *Exclusive Leptoproduction of ρ^0 Mesons from Hydrogen at Intermediate Virtual Photon Energies*, Eur. Phys. J. C17, (389-398), 2000. hep-ex/0004023.

[33] M. Diehl and S. Sapeta, *On the analysis of lepton scattering on longitudinally or transversely polarized protons*, Eur. Phys. J. C41, (515-533), 2005. hep-ph/0503023.

[34] F. Ellinghaus, W.-D. Nowak, A. V. Vinnikov, and Z. Ye, *Can the angular momentum of u-quarks in the nucleon be accessed in HERMES?*, 2005, hep-ph/0506264.

[35] E. R. Berger, F. Cano, M. Diehl, and B. Pire, *Generalized parton distributions in the deuteron*, Phys. Rev. Lett. 87, (142302), 2001. hep-ph/0106192.

[36] L. Mankiewicz, G. Piller, and T. Weigl, *Hard Exclusive Meson Production and Nonforward Parton Distributions*, Eur. Phys. J. C5, (119-128), 1998. hep-ph/9711227.

[37] M. Vanderhaeghen, P. A. M. Guichon, and M. Guidal, *Hard Electroproduction of Photons and Mesons on the Nucleon*, Phys. Rev. Lett. 80, (5064-5067), 1998.

[38] G. Baum et al., *COMPASS: A Proposal for a Common Muon and Proton Apparatus for Structure and Spectroscopy*, 1996, CERN-SPSLC-96-14.

[39] P. Abbon et al., *The COMPASS experiment at CERN*, Nucl. Instr. and Meth. A577, (455-518), 2007. hep-ex/0703049.

[40] M. Frhr. von Hodenberg, *A First Reconstruction of COMPASS Data*, Diploma thesis, Albert-Ludwigs-Universität Freiburg, June 2002.

[41] G. Abragam and M. Goldman, *Principles of dynamic nuclear polarisation*, Rep. Prog. Phys. 41, (395-467), 1999.

[42] E. Albrecht et al., *COMPASS RICH-1*, Nucl. Instr. and Meth. A502, (112-116), 2003.

[43] C. Bernet et al., *The COMPASS trigger system for muon scattering*, Nucl. Instr. and Meth. A550, (217-240), 2005.

[44] H. Fischer et al., *Implementation of the dead-time free F1 TDC in the COMPASS detector readout*, Nucl. Instr. and Meth. A461, (507-510), 2001.

[45] H. Fischer et al., *The COMPASS data acquisition system*, IEEE Trans. Nucl. Sci. 49, (443-447), 2002.

[46] Th. Schmidt, *A Common Readout Driver for the COMPASS Experiment*, PhD thesis, Albert-Ludwigs-Universität Freiburg, May 2002.

[47] A. Grünemaier, *Eine universelle Ausleseschnittstelle für das COMPASS-Experiment*, PhD thesis, Albert-Ludwigs-Universität Freiburg, September 2002.

[48] B. Grube, *The Trigger Control System and the Common GEM and Silicon Readout for the COMPASS Experiment*, Diploma thesis, Technische Universität München, December 2001.

[49] I. Konorov et al., *The Trigger Control System for the COMPASS Experiment*, Nuclear Science Symposium Conference Record, 2001 IEEE 1, (98-99), 2001.

[50] B. Gobbo, *CORAL web page*, http://coral.web.cern.ch/coral/.

[51] S. Gerassimov, *PHAST web page*, http://ges.home.cern.ch/ges/phast/.

[52] R. Brun and F. Rademakers, *ROOT web page*, http://root.cern.ch.

[53] P. Pagano, *Preliminary measurement of Transversity at COMPASS experiment*, PhD thesis, Universitá degli studi di Trieste, Anno Accademico 2001/02.

[54] K. Schoenning, *Study of the COMPASS spectrometer performance using K^0_S events*, Diploma thesis, University of Uppsala, 2003.

[55] E. S. Ageev et al., *A new measurement of the Collins and Sivers asymmetries on a transversely polarised deuteron target*, Nucl. Phys. B765, (31-70), 2007. hep-ex/0610068.

[56] J. Bisplinghoff et al., *Collins and Sivers asymmetries from COMPASS 2003/2004 transverse run*, March 2006, COMPASS Release Note.

[57] V. Alexakhine, *COMGEANT web page*, http://valexakh.home.cern.ch/valexakh/wwwcomg/.

[58] W.-M. Yao and other, *Review of Particle Physics*, J. Phys. G33, (1-1232), 2006. http://pdg.lbl.gov.

[59] A. Bressan, *Origin and cure of the peak in y*, April 2007, COMPASS note 2006-13.

[60] E. Burtin et al., *Angular distributions and $R = \sigma_L/\sigma_T$ for exclusive ρ^0 production*, May 2004, COMPASS Note 2004-12.

[61] P. Amaudruz et al., *Transverse Momentum Distribution for Exclusive ρ^0 Muonproduction*, Z. Phys. C54, (239-246), 1991.

[62] M. Alekseev et al., *Double spin asymmetry in exclusive ρ^0 muonproduction at COMPASS*, 2007, Accepted by Eur. Phys. J. C.; hep-ex/0704.1863.

[63] F. Bradamante and A. Martin, *Comparison between different proposed methods for the extraction of transverse spin asymmetries*, 2005, COMPASS Note 2005-5.

[64] K. Gustafsson, *Computation of the Dilution Factor for the Year 2002 COMPASS Data*, July 2003, COMPASS note 2003-3.

[65] B. Badelek, http://lxfsrb6103.cern.ch/compass/software/offline/input/dilfac/.

[66] J. Bisplinghoff et al., *Extraction of Transverse Target Single Spin Asymmetry for Exclusive ρ^0 Production from COMPASS 2002-2004*, August 2007, COMPASS note 2007-9.

[67] J. Bisplinghoff et al., *Collins and Sivers asymmetries on hadrons identified as pions and kaons from COMPASS 2003/2004 transvers run*, May 2006, COMPASS note 2006-12.

[68] K. Schilling and G. Wolf, *How to analyze vector meson production in inelastic lepton scattering*, Nucl. Phys. B61, (381-413), 1973.

Zusammenfassung

Nachdem lange Zeit vermutet wurde, der Spin des Nukleons ergebe sich als einfache Summierung der Helizitäten seiner Konstituenten, stellte das EMC Experiment in den 60er Jahre einen nur verschwindend geringen Beitrag dieser Helizitäten fest. Auch in folgenden, präziseren Messungen anderer Experimente ergab sich, dass der Beitrag der Quark-Helizitäten nicht ausreicht, um den Spin eines Nukleons vollständig zu beschreiben.

Mit modernen störungstheoretischen Methoden gelange es Jaffe und Manohar im Jahre 1992 eine Summenregel zu entwickeln, in der sich der Spin des Nukleons aus Beiträgen der Helizitäten der Quarks und Anti-Quarks $\Delta\Sigma$, der Helizitäten der Gluonen ΔG und deren Drehimpulse $L_{q,g}$ zusammensetzt:

$$\frac{1}{2}\hbar = \frac{1}{2}\Delta\Sigma + \Delta G + L_q + L_g \quad .$$

Bereits präzise bestimmt ist der Wert von $\Delta\Sigma$ und eine exakte Bestimmung von ΔG ist Ziel laufender Experimente. Wie jedoch die verbleibenden Drehimpuls-Beiträge zu bestimmen sind, war bislang völlig ungeklärt.

Im Jahre 1996 entdeckte man, dass generalisierte Parton-Verteilungen, zur Parametrisierung eines Nukleons in exklusiver tief-unelastischer Streuung verwendet werden können und dort vielfältige, bislang ungeahnte Möglichkeiten eröffnen, die Struktur der Nukleonen zu erforschen. Eine Schlüsselrolle erhält dabei eine Summenregel, die im Jahre 1998 in einer theoretischen Arbeit von Ji entwickelt wurde, in der die zweiten Momente der generalisierter Parton-Verteilungen E und H mit den totalen Drehimpulsen der Quarks im Nukleon verbunden sind.

Die exklusive Produktion von Mesonen, an einem bezüglich der Richtung des unpolarisierten (U) Strahls transversal-polarisierten (T) Targets, ist von besonderem Interesse, da die in diesem Prozess auftretende azimuthalen Asymmetrie $A_{\mathrm{UT}}(\phi_h - \phi_S)$ eine Extraktion der in Ji's Summenregel auftretenden generalisierten Parton-Verteilung E ermöglicht, die anderweitig nur schwer experimentell zugänglich ist. Die auftretenden Winkel ϕ_h und ϕ_S bezeichnen dabei die azimuthalen Winkel der Meson-Produktionsebene und des Target-Spin-Vektors bezüglich der Streuebene der Leptonen.

Ziel dieser Arbeit war die Extraktion der Amplitude $A_{\mathrm{UT}}^{\sin(\phi_h-\phi_S)}$ oben genannter Asymmetrie, in der exklusiven tief-unelastischen Produktion eines ρ^0-Mesons an einem transversal-polarisierten Deuteron-Target. Dabei sei die erstmalige Bestimmung dieser physikalischen Grösse betont, die durch Daten des COMPASS Experiments am CERN ermöglicht wurde, dem momentan weltweit einzi-

gen Experiment in dem die tief-unelastische Produktion von Mesonen an einem transversal-polarisierten Deuteron-Target untersucht werden kann.

Exklusive ρ^0-Meson Ereignisse wurden mittels eigens zu diesem Zweck geschriebenen Software selektiert und mit einem auf der Double-Ratio Methode basierenden Algorithmus konnte die Amplitude $A_{\mathrm{UT}}^{\sin(\phi_h-\phi_S)}$ der Asymmetrie $A_{\mathrm{UT}}(\phi_h-\phi_S)$ extrahiert werden, deren Wert sich auf

$$A_{\mathrm{UT}}^{\sin(\phi_h-\phi_S)} = 0.016 \pm 0.016(\mathrm{stat.})$$

beläuft und somit im Rahmen des statistischen Fehlers verträglich ist mit Null. Dieses Ergebnis betont die Notwendigkeit der Extraktion dieser physikalischen Grösse in unterschiedlichen kinematischen Bereichen, da einerseits die Gültigkeit theoretische Modelle zur Extraktion totaler Drehimpulse der Quarks im Nukleon aus diesen Ergebnissen begrenzt ist auf bestimmte kinematische Bereiche. Andererseits ergeben sich in unterschiedlichen kinematischen Breichen, unterschiedliche Sensitivitäten der Amplitude auf spezielle Beiträge. So ist beispielsweise der Bereich höherer Virtualität des wechselwirkungs-übertragenden Photons im höheren Maße sensitiv auf die Produktion eines ρ^0-Mesons, ausgelöst durch ein longitudinal-polarisiertes Photon. Die Photon-Polarisation ist dabei essentiell, da eine Beschreibung des Nukleons unter Verwendung von generalisierten Parton-Verteilungen nur für longitudinal-polarisierte Photonen gültig ist.

Diese erste Extraktion von $A_{\mathrm{UT}}^{\sin(\phi_h-\phi_S)}$ bietet Raum für weiterführende Studien, deren Hauptmerkmale darin bestehen könnten, vorhandene Beimischungen von nicht-exklusivem Untergrund zu bestimmen, dessen Beitrag grob zu etwa 20% abgeschätzt wurde. Zudem enthälten der ausgewählten Daten-Satz Beiträge von Ereignissen in denen Mesonen unter Austausch transversal-polarisierter Photonen produziert wurden. Einen dritten Beitrag stellen sogenannte kohärent-produzierten ρ^0-Mesonen dar, bei deren Produktion das Target-Deuteron nach dem Streuprozess intakt bleibt und somit eine Parameterizierung eines individuellen Nukleons, d.h. des Protons oder Neutrons, im Deuteron nicht möglich ist.

Seit Mitte diesen Jahres verwendet das COMPASS Experiment ein transversal-polarisiertes Proton Target. Aus diesen Messungen ist wiederum die Extraktion der Amplitude $A_{\mathrm{UT}}^{\sin(\phi_h-\phi_S)}$ möglich. Zudem können diese Ergebnisse in Kombination mit den vorliegenden Ergebnissen verwendet werden, um Informationen über die Struktur des Neutrons zu erlangen. In fernerer Zukunft wird eine Erweiterung des experimentellen Aufbaus die Messung der tief-unelastischen Compton Streuung erlauben, einem weiteren experimentellen Zugangs zu generalisierten Parton Verteilungen. COMPASS trägt somit bei, das fehlende Wissen über die Beiträgen zum Spin des Nukleons immer weiter zu vervollständigen.

Acknowledgments

Constant support and advices of many people have lead to the successful completion of this work. In particular I would like to say **Thank you!** to the people that follow:

- First of all I would like to thank Prof. Kay Königsmann for giving me the opportunity to join the group and become part of the COMPASS collaboration. Moreover, his pleasant calm and continual interest in the progress of my work was always encouraging.

- For all his advices, support and help I would like to thank my supervisor Prof. Horst Fischer. Beside physics, I learned a great deal about the scientific life, a lesson I never imagined to learn but which I'm more than grateful for. **Thanks** for you excellent supervision.

- All my colleagues in Freiburg, are due a special thanks for their good professional and personal co-operation. Thanks to Jochen Barwind, Wolfgang Käfer, Andreas Mutter, Frank Nerling and Christian Schill, who partly (and one of them fully) read the drafts of this thesis. Moreover thanks to Roland Hagemann and Andreas Mutter again for being my saviors, in times of Murphy's reign over my computer.

- I would like to thank Nicole d'Hose, Etienne Burtin and Andrej Sandacz for a lot of fruitful discussions about Generalized Parton Distributions, exclusive processes and all that stuff. Thanks also to Guillaume Jegou with whom a successful X-Check and publishing of results was achievable.

- Apart from all that physics, there is one person deserving a huge **Thank You!** for helping in completing this thesis. Richard von der Heyde has to be named, who above all was calmly and professionally reading my thesis and showed me the wondrous world of a foreign language: English.

- A lovely thanks to my family for making all my studies possible even when sometimes this physics stuff was all around and every day life seems full of spins and particles. Without your constant love and support, not the slightest success would have been possible during my studies: **Thank you!**

- Finally I would like to thank Moritz Gruschke for his constant support and love. You were the helping hand for me in reading, discussing and sometimes in just being there when things where not that easy. Without you none of this would have come that far. You were the one completing it. A heartfelt **thank you** for everything.

Erklärung

Diese Arbeit is von mir selbstständig verfasst worden, und ich habe keine anderen als die angegebenen Quellen und Hilfsmittel benutzt.

Jasmin Kiefer, August 2007.